Use of Cloud Radar Doppler Spectra to Evaluate Stratocumulus Drizzle Size Distributions in Large-Eddy Simulations with Size-Resolved Microphysics

J. RÉMILLARD,[a] A. M. FRIDLIND,[b] A. S. ACKERMAN,[b] G. TSELIOUDIS,[b] P. KOLLIAS,[a,c] D. B. MECHEM,[d] H. E. CHANDLER,[d] E. LUKE,[c] R. WOOD,[e] M. K. WITTE,[f] P. Y. CHUANG,[f] AND J. K. AYERS[g]

[a] *Stony Brook University, State University of New York, Stony Brook, New York*
[b] *NASA Goddard Institute for Space Studies, New York, New York*
[c] *Brookhaven National Laboratory, Brookhaven, New York*
[d] *University of Kansas, Lawrence, Kansas*
[e] *University of Washington, Seattle, Washington*
[f] *University of California, Santa Cruz, Santa Cruz, California*
[g] *Science Systems and Applications, Inc., and NASA Langley Research Center, Langley, Virginia*

(Manuscript received 10 April 2017, in final form 26 July 2017)

ABSTRACT

A case study of persistent stratocumulus over the Azores is simulated using two independent large-eddy simulation (LES) models with bin microphysics, and forward-simulated cloud radar Doppler moments and spectra are compared with observations. Neither model is able to reproduce the monotonic increase of downward mean Doppler velocity with increasing reflectivity that is observed under a variety of conditions, but for differing reasons. To a varying degree, both models also exhibit a tendency to produce too many of the largest droplets, leading to excessive skewness in Doppler velocity distributions, especially below cloud base. Excessive skewness appears to be associated with an insufficiently sharp reduction in droplet number concentration at diameters larger than ~200 μm, where a pronounced shoulder is found for in situ observations and a sharp reduction in reflectivity size distribution is associated with relatively narrow observed Doppler spectra. Effectively using LES with bin microphysics to study drizzle formation and evolution in cloud Doppler radar data evidently requires reducing numerical diffusivity in the treatment of the stochastic collection equation; if that is accomplished sufficiently to reproduce typical spectra, progress toward understanding drizzle processes is likely.

1. Introduction

Drizzle exerts a major influence on the evolution of stratocumulus clouds via changes to boundary layer stratification, cloud cover, and mesoscale structure (e.g., Stevens et al. 1998; Savic-Jovcic and Stevens 2008; Wang and Feingold 2009). The drizzle process also depletes cloud condensation nuclei (CCN) from the cloud-topped boundary layer via collision–coalescence scavenging (e.g., Ackerman et al. 1993, 1994; Feingold et al. 1996; Mechem et al. 2006; Wood 2006; Koren and Feingold 2011).

Despite its importance, drizzle representation in weather and climate models remains rather weakly constrained by observations (e.g., Suzuki et al. 2011, 2013). One path to generation and improvement of drizzle parameterizations is via analysis of large-eddy simulation (LES) results with size-resolved (bin) microphysics (e.g., Khairoutdinov and Kogan 2000). However, differing models may yield substantially differing predictions of drizzle intensity for any given case study (Ackerman et al. 2009), apparently owing to differing treatments of bin microphysics or dynamics or both.

Using observations to constrain drizzle behavior in simulations is difficult for two leading reasons. First, cloud properties such as liquid water path (LWP), understood to be important to drizzle formation, exhibit substantial variability across a wide range of scales, generally much broader than reproduced in any given simulation (as exemplified below). Second, whether using in situ or remote sensing measurements or a combination of both, cloud properties most useful for constraining simulation behavior are difficult to sample, especially collocated variables at the most relevant scales. Examples include collocated, three-dimensional fields of cloud droplet and drizzle size distributions and dynamics (flow properties). Thus, although it would be ideal to directly

Corresponding author: A. M. Fridlind, ann.fridlind@nasa.gov

DOI: 10.1175/JAMC-D-17-0100.1

evaluate the simulated three-dimensional evolution of a drizzling, cloud-topped boundary layer, statistically persuasive direct comparison is not possible with current observational assets.

The present study takes the more limited approach of using cloud Doppler radar observations to constrain simulated drizzle properties (the state of drizzle observable by Doppler radar). The profiling cloud radar employed in this study samples the state of cloud and drizzle properties but not the time-dependent evolutionary process of drizzle formation. Nevertheless, this work is intended as a foundational step to using cloud Doppler radar observables to broadly constrain drizzle properties in models and, via observational inference, to advance understanding of drizzle formation. We refer to the approach as foundational because it is a first attempt (to our knowledge) to systematically compare Doppler spectra from cloud radar with spectra derived from LES. Our method of approaching this foundational step is motivated by the fact that relationships between cloud Doppler radar observables exhibit relatively stable statistics over a wide range of conditions (Kollias et al. 2011). This relative stability of drizzle property relationships supports the use of a case-study approach despite the understanding that the observed mesoscale variability of LWP, for example, will not be reproduced. We therefore ask the relatively limited question: Are the simulations able to reproduce the statistically robust relationships among cloud radar observables found in observations?

This study focuses on a case study of drizzling marine stratocumulus cloud (described in section 2) with several sensitivity tests. The case study is simulated with two independent LES codes with independent bin microphysics schemes (described in section 3). Simulation results are first compared with one another and with observed variables such as LWP (section 4a). The drizzle size distributions are then investigated in greater detail through Doppler radar observations and limited in situ measurements from another observational dataset (section 4b). Last, the results are discussed and future work is outlined (section 5).

2. Case description

The Clouds, Aerosols, and Precipitation in the Marine Boundary Layer (CAP-MBL) campaign deployed a U.S. Department of Energy Atmospheric Radiation Measurement (ARM) mobile facility for 19 months over the Azores, resulting in a wealth of collocated aerosol, cloud, radiation, and meteorological observations (Wood et al. 2015). Using weather state classification from International Satellite Cloud Climatology Project data (Tselioudis et al. 2013), the selected case study is identified as one when stratocumulus types prevailed for an extended period of time (>10 h) on 22 November 2009 (Rémillard and Tselioudis 2015, their Fig. 10) beneath a strong Azores high. Satellite imagery indicates stratocumulus fields covering a large area around the Azores (Fig. 1). Rémillard and Tselioudis (2015) also show that this weather state is substantially underrepresented in simulations from many climate models.

Vaisala, Inc., RS92 radiosondes from Graciosa reveal a relatively well-mixed boundary layer topped by a strong inversion around 1.6 km (Fig. 2). This structure was observed throughout the day, with a slight increase in boundary layer specific humidity during daytime. Light westerly winds prevailed with limited shear, the strongest component being $\sim 5\,\mathrm{m\,s^{-1}}$ in the northerly wind across the top of the boundary layer. Combining measurements from the W-band ARM cloud radar (WACR; Mead and Widener 2005) with cloud-base height from a Vaisala CL25K ceilometer (Münkel et al. 2007) illustrates active precipitation in the form of drizzle size drops throughout the day, although negligible drizzle reached the surface (see Fig. 2e). Those measurements also confirm the presence of mesoscale variability, with episodes of thin clouds alternating with more heavily drizzling periods.

3. Simulations

a. Models

The Distributed Hydrodynamic Aerosol and Radiative Modeling Application (DHARMA) LES represents three-dimensional turbulent fluid flow using a forward-in-time projection method and a third-order advection scheme for both velocity and scalar advection (Stevens et al. 2002). A dynamic Smagorinsky scheme treats sub-grid-scale mixing (Kirkpatrick et al. 2006). Dynamics are advanced with a 5-s time step, which is shortened when required to maintain a maximum Courant number for the resolved flow of 0.8. A sponge layer damps interactions with the model lid using a time scale of 100 s and a strength varying as the square of a sinusoid ($\sin^2$) from zero at 2 km to unity at 2.5 km.

In DHARMA, the LES code is coupled with a modified version of the Community Aerosol-Radiation-Microphysics Application (CARMA) size-resolved microphysics model (Ackerman et al. 1995; Jensen et al. 1998). Droplet nucleation (aerosol activation), condensational growth, and evaporation are advanced using localized time splitting, with a minimum microphysics time step of 0.02 s, whereas particle sedimentation and collision–coalescence are advanced using the LES dynamics time step. Droplet condensational growth and

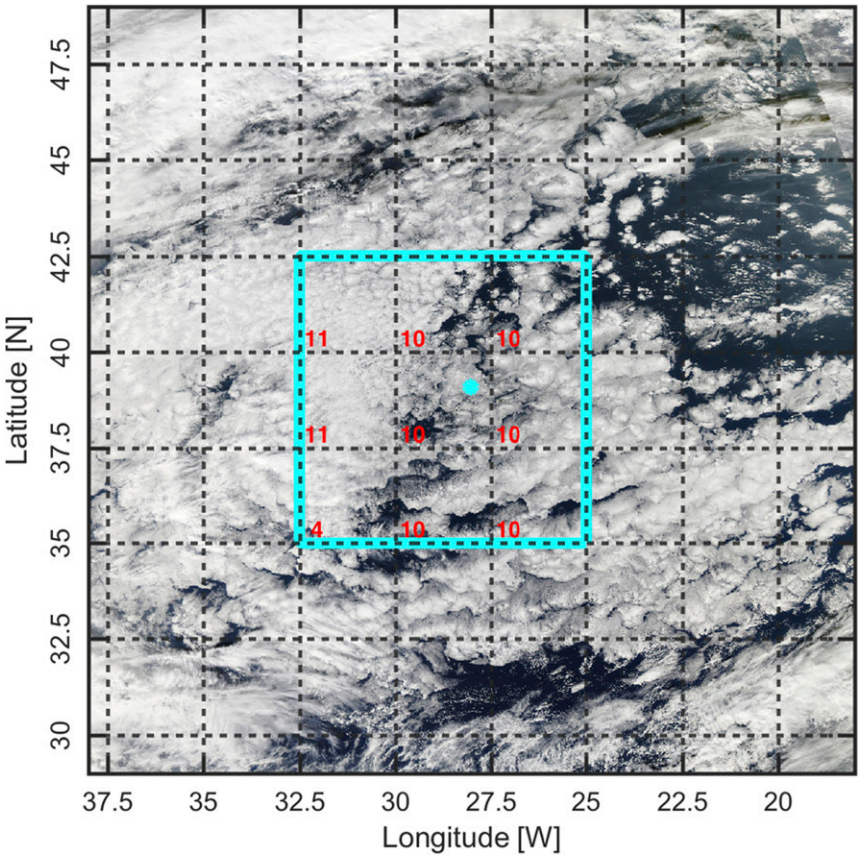

FIG. 1. *Aqua* MODIS 20° composite true color image at 1505 UTC 22 Nov 2009 centered on Graciosa (cyan dot). Red numbers are the states of weather assigned to 2.5° cells (see Rémillard and Tselioudis 2015), where 10 and 11 indicate stratocumulus conditions.

evaporation are treated with the piecewise parabolic method of Colella and Woodward (1984), and sedimentation is treated using first-order upwinding, sub-stepped to maintain stability with respect to the sedimentation Courant number. The stochastic collection equation, which treats autoconversion, accretion, and drizzle self-collection in a continuous fashion in size-resolved microphysics schemes, is solved using a mass-conserving semi-implicit algorithm (Jacobson et al. 1994). Hydrometeor fall speeds and pairwise collision and coalescence rates are calculated following Böhm (1999, 2004, and references therein), wherein the aspect ratio of large drops follows Green (1975). The coalescence efficiency is assumed to be unity for all collisions; results and conclusions are not sensitive to instead assuming Beard and Ochs (1984) coalescence efficiencies (not shown).

The System for Atmospheric Modeling (SAM)–Explicit Microphysics (SAMEX) derives from the anelastic dynamical core used in the SAM (Khairoutdinov and Randall 2003) and has been employed in a number of studies of boundary layer clouds (VanZanten et al. 2011; Kogan et al. 2012; Mechem et al. 2012, 2015). Momentum advection is calculated using third-order Adams–Bashforth time differencing and second-order spatial finite differences based on the flux form of the momentum equation. The scalar advection routine uses the multidimensional positive-definite advection transport algorithm of Smolarkiewicz and Grabowski (1990). Sub-grid-scale fluxes in SAMEX are parameterized using the 1.5-order scheme of Deardorff (1980). Dynamics are advanced with a 2-s time step.

The explicit (bin) representation of microphysical processes in SAMEX is based on Kogan (1991) and includes size-resolving representations of liquid water and hygroscopic aerosol (25 and 19 bins, respectively). Microphysics processes are advanced with a 0.2-s time step. As in DHARMA, the droplet spectrum in SAMEX is represented by a single-moment mass distribution function. Condensation and evaporation employ a semi-Lagrangian approach and the variational optimization method of Liu et al. (1997) to remap the drop spectrum

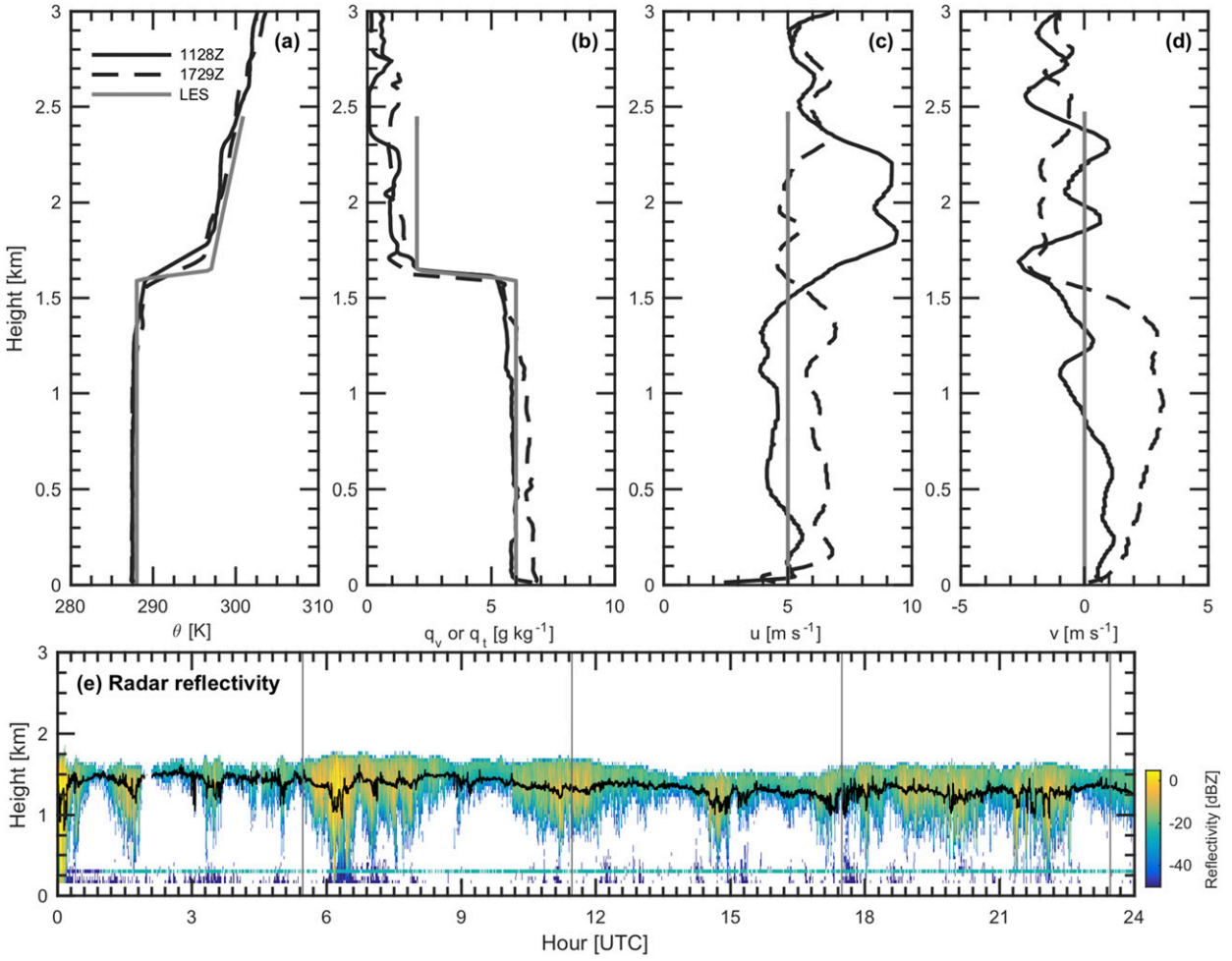

FIG. 2. Vertical structure of the boundary layer on 22 Nov 2009 from daytime radiosondes (1130 UTC in solid and 1730 UTC in dashed lines) and as used to initialize the simulations (gray lines): (a) potential temperature, (b) measured water vapor or initial total water mixing ratio, (c) zonal wind speed, and (d) meridional wind speed. (e) Observed radar reflectivity with ceilometer CB height (black line) and sounding launch times (vertical gray lines).

to the Eulerian bins. The stochastic collection equation is computed by the method of Berry and Reinhardt (1974). Drop fall speeds follow Berry and Pranger (1974). All simulations use the Hall (1980) collection kernel and assume a coalescence efficiency of unity.

Both models use the same vertical domain extent (2.5 km) and grid mesh configuration, which is finest at the surface and at cloud top (~10 m). A 9.6 km × 9.6 km domain with 100-m horizontal grid spacing was initially used by both models, but it was later refined for many DHARMA sensitivity tests to a 4.8 km × 4.8 km domain using 75-m grid spacing, with only a negligible change in results (only smaller domain simulations are included here; see Table 1).

In both models, liquid hydrometeors are represented by a mass-doubling bin array, where the smallest bin represents droplets of 2-μm diameter. In SAMEX, 25 bins are used, whereas DHARMA uses 35 bins to avoid the possibility of accumulation in the largest bin. An array of 60 bins is alternatively used in some DHARMA sensitivity tests with a mass ratio of $2^{1/2}$ between successive bins. This test is made in order to reduce numerical diffusion associated with collision–coalescence, a known source of model error. Code design limitations prevent such sensitivity tests for SAMEX.

In both models, multimodal aerosols are treated diagnostically following Clark (1974) in order to avoid the challenges associated with properly representing aerosol source terms and the regeneration of aerosol following droplet evaporation. Aerosol activation is treated by transferring available aerosol into a droplet bin wherever supersaturation exceeds the critical supersaturation of an aerosol bin. For DHARMA, dry

TABLE 1. Summary of simulations with varying total aerosol number concentration (N_a) and mass ratio between consecutive droplet bins (lower mass ratio corresponds to finer spectral resolution).

Model	Domain size	N_a (cm^{-3})	Bins	Mass ratio	Simulation name
DHARMA	5 km × 5 km	260	35	2	DHARMA260
		130	35	2	DHARMA130
		130	60	1.4	DHARMA130b
		65	60	1.4	DHARMA065b
SAMEX	10 km × 10 km	260	25	2	SAMEX260
		130	25	2	SAMEX130

aerosol are transferred into the smallest droplet bin that accommodates the aerosol (always the first bin for these CCN), and by virtue of a large solute effect, moisture is taken up rapidly via diffusional growth. For SAMEX, activated aerosol are transferred into the cloud droplet bin corresponding to the wet (deliquesced) CCN size, which for these CCN will be predominantly the smallest droplet bin. At each time step, available aerosol are set to the initial size distribution less the number of droplets within the grid cell, subtracted cumulatively from largest to smallest aerosol bin. Any reduction in the sum of droplet and aerosol concentration by collision–coalescence is thus effectively offset by increasing aerosol number by the same amount. The Clark (1974) approach is commonly used to represent quasi-steady-state aerosol conditions without characterizing aerosol source terms (e.g., Ackerman et al. 2004).

b. Simulation setup

Simulations are initialized with the CAP-MBL Azores sounding from 1130 UTC 22 November 2009, subject to some idealization to simplify further investigation (see Fig. 2). Despite the variety of instruments deployed during the CAP-MBL campaign, no observational estimate of the large-scale forcings is available. The subsidence profile is therefore based loosely on European Centre for Medium-Range Weather Forecasts interim reanalysis data (Dee et al. 2011), adjusted to obtain a boundary layer depth and cloud-top height evolution similar to the observations during 6-h simulations: zero at the surface, increasing linearly with height to 0.48 cm s^{-1} at 1600 m (consistent with a uniform horizontal divergence of 3×10^{-6} s^{-1}), and fixed at that value above. For simplicity and to reduce sources of divergence between the two models, longwave radiative transfer is parameterized as a function of liquid water content following Beer's law (cf. Larson et al. 2007), and shortwave radiative transfer is neglected; the extinction coefficient and net fluxes above cloud and at the surface are as in Ackerman et al. (2009), with the clear-sky term above the inversion omitted. Horizontal winds are nudged to their initial profiles with a 2-h time scale and strength that scales vertically as $\sin^2$ from zero at 2 km to unity at the domain top. Water vapor mixing ratio and potential temperature are nudged with a 2-h time scale and a strength that scales vertically as $\sin^2$ from zero at the surface to unity at the domain top. Surface turbulent fluxes are treated using the approach of Ackerman et al. (2009). Namely, sensible and latent heat fluxes are fixed to 0 and 95 W m^{-2}, and friction velocity is fixed to 0.16 m s^{-1} based on quasi-steady-state values predicted interactively in DHARMA from sea surface roughness under the specified wind conditions and a sea surface temperature of 290.4 K.

We use the aerosol observing system (AOS) measurements taken near ground level on Graciosa to estimate CCN initial conditions. Figure 3 shows CCN measurements from 0600 to 1800 UTC, corrected for bias based on collocated condensation nucleus measurements (Wood et al. 2017), and their statistics when binned according to their supersaturation value. A fit with two lognormal modes of ammonium bisulfate is performed, minimizing the root-mean-square difference between the computed and median values in each bin, putting more weight on the lower supersaturation values. The resulting aerosol number distribution is also shown in Fig. 3, with modes at radii of 20 and 50 nm, respective geometric standard deviations of 1.1 and 1.4, and number concentrations of 150 and 370 cm^{-3}. Because so many aerosol particles would yield droplet concentrations of roughly 300 cm^{-3} following Abdul-Razzak and Ghan (2000) with the convection strength demonstrated below, inconsistent with drizzle observed throughout even thin cloud periods, we halved those numbers such that a total aerosol number concentration of 260 cm^{-3} is used for our baseline simulations (specified as vertically uniform modal mixing ratios of 65 and 162.5 mg^{-1}), and sensitivity tests use lesser values, with both modes scaled accordingly (see Table 1).

4. Results

a. Drizzle context

To assess the resemblance of the simulations to observations of the case-study period, domain-averaged time series of simulations are shown in Fig. 4. Here, we take 0900 UTC as a start time for comparison with observations in order to include a range of observed drizzle conditions around 1130 UTC; simulations neglect solar radiation and large-scale forcing evolution and are therefore loosely bound to observation time. Continuous cloud fraction, boundary layer depth, LWP, and cloud droplet number concentration (N_d) diagnostics

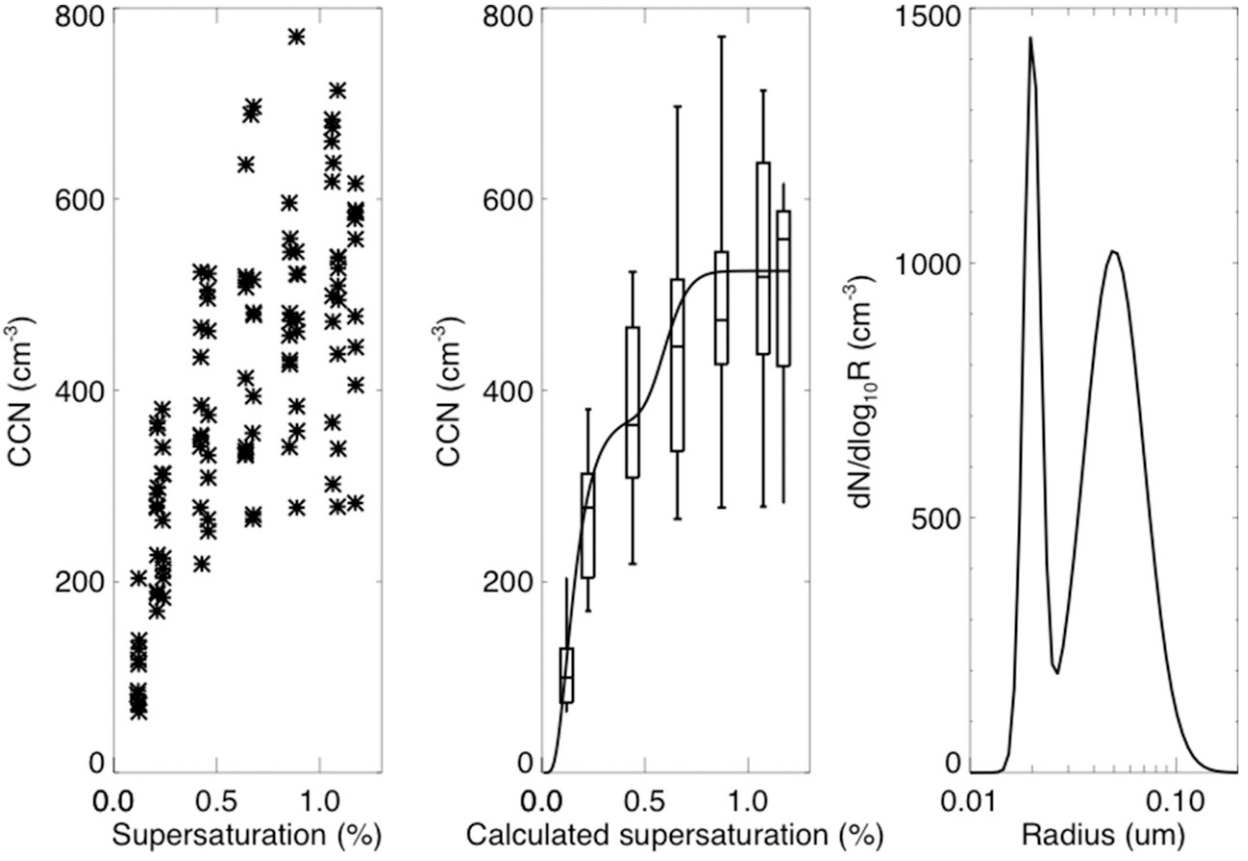

FIG. 3. (left) CCN data obtained from 0600 to 1800 UTC 22 Nov 2009 as corrected for instrument noise and agreement with CN observations (Wood et al. 2017). (center) Box plots of medians, upper and lower quartiles, and extrema of the same data binned by supersaturation, with the line fit to a bimodal aerosol. (right) Aerosol number size distribution corresponding to the fit.

are shown for the six hours simulated. Cloud-base precipitation rate (P_{cb}) and cloud-top effective radius (r_e) are shown with their standard deviations for the last two hours of simulation time, as calculated offline from three-dimensional (3D) output fields. Columnwise cloud base in the simulation analysis is defined as the bottom of the lowest grid cell where visible extinction exceeds $0.001\,m^{-1}$, considering only hydrometeors and treating them as conservative, geometric scatterers. Also shown for the simulated six hours are satellite retrievals of cloud fraction, LWP, N_d, and r_e using the visible infrared shortwave–infrared split window technique (VISST; Minnis et al. 2011).

Ground-based measurements of cloud cover from a total sky imager (TSI; Long and DeLuisi 1998) are seen in Fig. 4a to indicate continuous cloud cover, consistent with radar and ceilometer measurements in Fig. 2, and satellite retrievals. All simulations also maintain fully overcast conditions, as well as steady boundary layer depth consistent with that derived from the initial sounding (Fig. 4b). However, mesoscale variability not captured by the simulations is also evident in ground-based and satellite retrievals. In particular, LWP values retrieved from a ground-based Radiometrics Corporation microwave radiometer (MWR; Turner et al. 2007) and from passive satellite retrievals commonly range over roughly 25–150 $g\,m^{-2}$, as demonstrated by both hourly statistics and large associated standard deviations (Fig. 4c). By contrast, all simulations show a steady increase of domain-mean LWP after spinup (1–2 h) from roughly 75 to 100 $g\,m^{-2}$. A similar but more rapid increase is seen in the observations from 0930 to 1130 UTC, which we attribute to mesoscale variability and a region of large LWP passing over the site. Owing to a similar range and trend in LWP, this period will be the focus of some comparisons below.

Since the LWP evolution is nearly identical in all simulations, the differences in assumed aerosol are ultimately responsible for differences in simulated P_{cb} in each model (Fig. 4d). Furthermore, regardless of assumed aerosol, the median P_{cb} in every DHARMA simulation is lower by nearly an order of magnitude than in any SAMEX simulation despite the fact that DHARMA N_d spans SAMEX N_d (see Fig. 4). With

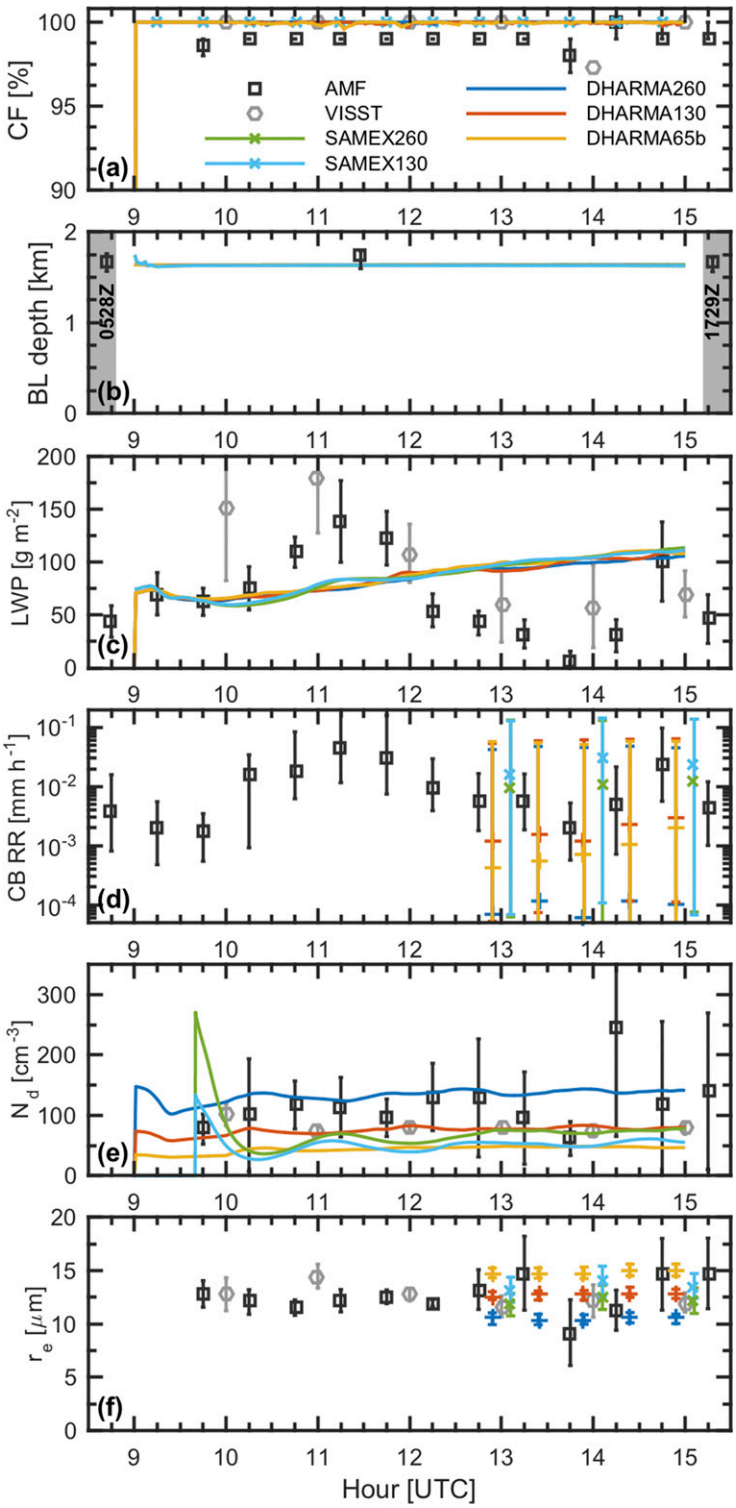

FIG. 4. Time series of simulated domain-averaged (a) cloud fraction, (b) boundary layer depth, (c) LWP, (d) P_{cb}, (e) N_d, and (f) r_e, where P_{cb} and r_e are shown with standard deviations derived from 3D output fields (see text). Simulation symbols are slightly offset in time for legibility. Observations are 30-min ground based (black symbols) and hourly satellite based (gray symbols), where vertical bars denote the standard deviations, except in (d) where they represent the 5th–95th-percentile range, and the symbols indicate the median values. Ground-based retrievals were obtained from TSI in (a), from analysis of 6-hourly soundings in (b), from MWR in (c), from radar and ceilometer in (d), and from MFRSR in (e) and (f) (see text).

TABLE 2. Simulated LWP, droplet number concentration (N_d), CB precipitation rate (P_{cb}) and standard deviation of vertical wind at CB (σ_w) and predicted values of N_d and P_{cb} following Abdul-Razzak and Ghan (2000) and Comstock et al. [2004, their Eq. (17)].

Simulation name	LWP (g m^{-2})	N_d (cm^{-3})	P_{cb} (mm day^{-1})	σ_w (m s^{-1})	Predicted N_d (cm^{-3})	Predicted P_{cb} (mm day^{-1})
DHARMA260	100	139	0.02	0.66	177	0.21
DHARMA130	101	79	0.07	0.65	94	0.55
DHARMA130b	104	83	0.02	0.68	95	0.55
DHARMA065b	105	48	0.04	0.66	58	1.2
SAMEX260	106	74	0.19	0.55	176	0.70
SAMEX130	105	54	0.34	0.54	92	1.2

nearly identical LWP and varying N_d values simulated, the Comstock et al. (2004) Z–R relationship gives P_{cb} of at least 3 times as great as SAMEX and 10 times as great as DHARMA over all simulations (Table 2). Figure 5 places the simulations from this study into the context of some field observations, past published DHARMA simulations that use a mass ratio of 2.4 between successive bins (Ackerman et al. 2004), and the Comstock et al. (2004) relation. The Ackerman et al. (2004) DHARMA simulations are seen to roughly follow the Comstock et al. (2004) relation, whereas the DHARMA260, DHARMA260b, and DHARMA130b simulations (see Table 1) are outlying low values, and the remaining simulations lie roughly within the lower envelope of observations. Increasing the DHARMA mass ratio to 2.4 as in Ackerman et al. (2004) increases P_{cb} by roughly a factor of 2 (not shown), indicating that closeness of agreement with the Comstock et al. (2004) relation is at least partly case-study dependent. The uncertainty associated with collision–coalescence schemes, the computational expense of fully converged solutions, and the generally good agreement with observations using a mass ratio of 2.4 motivated use of that mass ratio in past simulations; attempting to improve agreement of simulated and observed Doppler spectra motivates reduction of the mass ratio to 1.4 in the DHARMA130b and DHARMA65b simulations here. None of the simulations include enhancement of collision–coalescence by turbulence, which could conceivably enhance derived autoconversion by a factor of 1.25–3 (Hsieh et al. 2009), or other proposed improvements to collision–coalescence treatment that would generally increase drizzle formation rates, as discussed further below.

The first-order influence of changing aerosol number concentration is notably stronger in DHARMA than in SAMEX insofar as N_d nearly doubles when doubling aerosol concentration in DHARMA but only modestly increases in SAMEX (Fig. 4e and Table 2). When 260 cm^{-3} aerosols are initially assumed based on surface observations, DHARMA also predicts nearly twice as many droplets as SAMEX, associated with a P_{cb} that is roughly two orders of magnitude smaller than both SAMEX and observations. One possible explanation for differences of N_d in DHARMA260 versus SAMEX260 simulations is tied to differences in vertical motions driving supersaturation and droplet activation. Figure 6 shows the domain-averaged vertical structure over the last simulated hour. All simulations develop very similar profiles of temperature, humidity, and horizontal winds. DHARMA simulates a more active boundary layer, consistent with activation of more droplets (Fig. 6d), but this difference is not responsible for the disparity in the number of drops produced, as DHARMA sensitivity tests designed to yield vertical wind speed variance similar to SAMEX yielded little change in simulated N_d (not shown). Using Abdul-Razzak and Ghan (2000) to make offline calculations of N_d using DHARMA's vertical wind speed variance near cloud base yields N_d closer to that predicted in DHARMA simulations and supports the weak dependence of N_d on vertical wind speed variance (Table 2). We note that LES

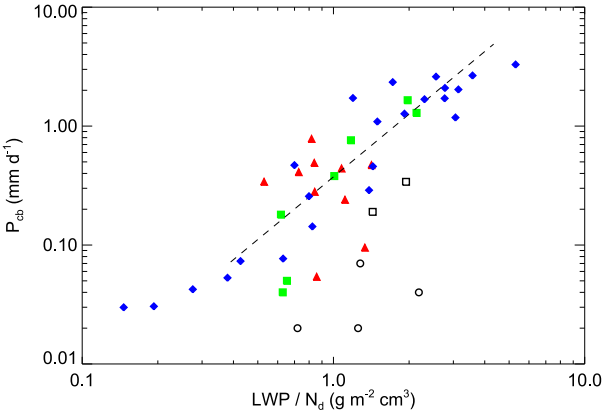

FIG. 5. The CB precipitation rate (P_{cb}) as a function of LWP divided by cloud droplet number concentration (N_d) as simulated in this study by DHARMA (open circles; see Table 2) and SAMEX (open squares), fit to observations by Comstock et al. [2004, their (Eq. 17); dashed line], derived from observations by VanZanten et al. (2005) and Stevens et al. (2003) (green symbols) and Wood (2005; single-layer cases; red symbols), and simulated using DHARMA by Ackerman et al. (2004; blue symbols).

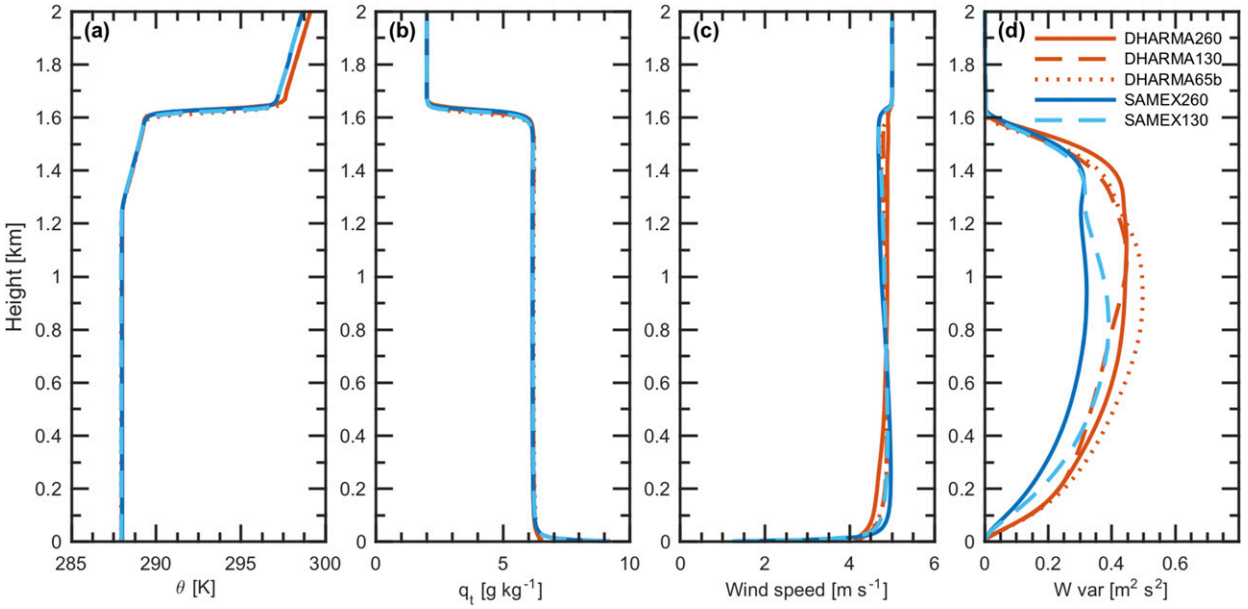

FIG. 6. Profiles of (a) potential temperature, (b) total water mixing ratio, (c) horizontal wind speed, and (d) vertical wind speed variance averaged over the last hour of simulations.

intercomparison studies commonly fix N_d and have not generally tested model ability to predict this first-order response of hydrometeor fields to aerosol; to our knowledge, no study has focused on such a test of LES prediction of N_d to date.

In the DHARMA260 simulation, N_d remains within the range of some ground-based retrievals from a multifilter rotating shadowband radiometer (MFRSR; Harrison et al. 1994) but is roughly 50% greater than values computed from satellite retrievals. The DHARMA260 r_e of roughly 10 μm is generally just below the range of most ground-based and satellite retrievals. In the SAMEX260 simulation, on the other hand, N_d and r_e agree quite closely with the satellite retrievals, and P_{cb} also agrees more closely with ground-based retrievals when LWP is similar to observed, as discussed further below.

In summary thus far, we find that DHARMA and SAMEX simulations yield essentially identical LWP but grossly differing N_d that cannot be explained by differences in dynamics, as well as grossly differing sensitivity of N_d to halving aerosol concentration. We note that it was ensured that critical supersaturations as a function of aerosol size match in the two models. Thus, other differences in numerical schemes are assumed responsible for differences in predicted N_d. Future tests of model activation codes could be made in parcel mode, but that capability does not currently exist in the SAM code. Whereas DHARMA260 N_d and sensitivity of N_d to halving aerosol agree better with Abdul-Razzak and Ghan (2000) in offline calculations, the SAMEX260 simulation agrees better with the full complement of surface CCN and satellite-retrieved N_d and cloud-top r_e. Although it was not the intention of this study to delve deeply into these relationships, this knowledge of the differences between observed and simulated bulk cloud properties may be useful in explaining differences in the observed and simulated cloud radar spectra. Potential causes of model differences across all results are further discussed in section 5.

b. *Drizzle properties*

Figure 7 shows the occurrence frequencies of cloud-base and cloud-top heights as well as the distance reached by drizzle beneath the cloud base, as binned by radar range gate, with vertical resolution of ~45 m. Simulated values are calculated offline from 3D fields over the last two hours of simulation time as in Fig. 4. Observed values are taken over the whole day and for the subperiod 0900–1500 UTC shown in Fig. 4. Overall, observations show broader distributions of cloud-base and cloud-top heights from mesoscale variability that is not reproduced in the simulations, but the simulated values generally lie within 100 m of typically observed values. However, simulated drizzle reaches deeper below cloud base than observed, especially in DHARMA (Fig. 7c). By contrast, only a relatively small fraction of SAMEX drizzle occurrences reach depths that are outside of the observed range.

To further compare simulated and observed radar Doppler moments and spectra, a forward simulator is

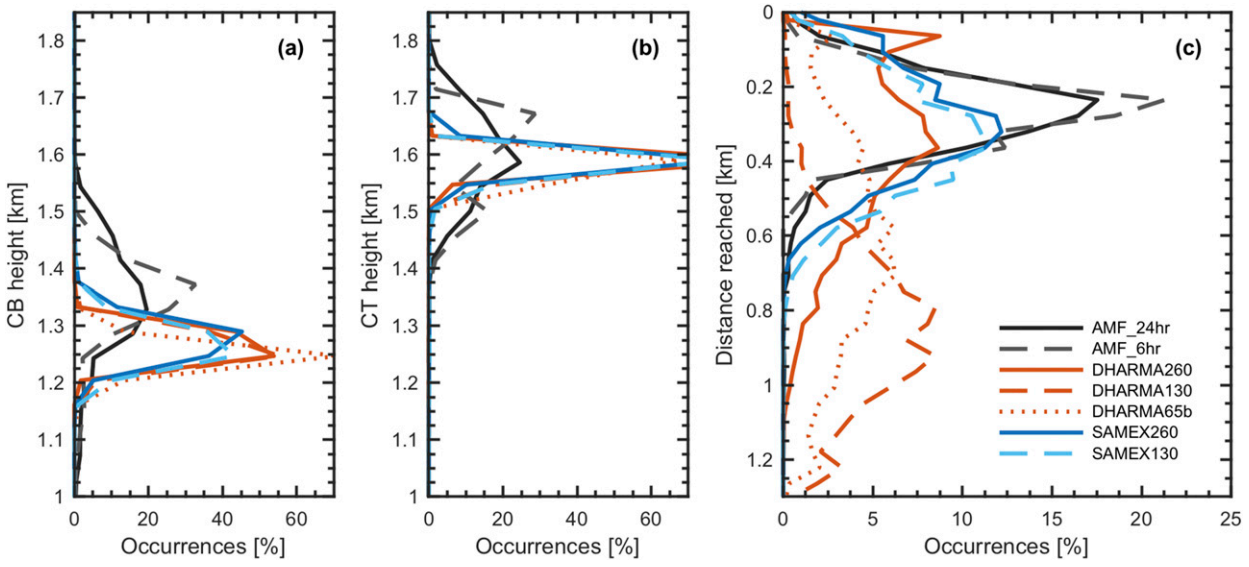

FIG. 7. Distributions of (a) CB and (b) cloud-top heights as retrieved from the ceilometer and radar observations (black solid and dashed lines for 24- and 6-h observation periods, respectively; see text) and from the simulations (see legend). (c) Distributions of the distance reached by the drizzle below CB as defined by reflectivity threshold (see text).

applied to the 3D model output fields (see appendix A). For illustrative purposes, because model results are not saved at every time step, curtain plots are generated from each simulation by selecting profiles along a path through each input field (Fig. 8). In each simulation field, a constant horizontal wind is assumed throughout the column, fixed at the value found near cloud base. The corresponding time variable is estimated by dividing the distance between the points by this speed. Concatenating profiles from all full-domain fields produces an apparent continuous time series of profiles similar to what might be observed by a radar.

Figure 8a illustrates the 0900–1200 UTC period of observations when LWP increases to values similar to that during the last two hours of simulations. This period represents well the two main regimes present in observations throughout the day. The first is a thin, weakly drizzling regime (first hour), with reflectivity remaining low (around $-20\,\mathrm{dB}Z$) and only limited drizzle below cloud base. The second is a more active regime with higher reflectivity values that are maximum near cloud base and with drizzle consistently reaching deeper below cloud base. Simulated LWP, which varies little across all simulations, most closely resembles that observed at roughly 1100 UTC (see Fig. 4c).

Figures 8b–g show reflectivity for all simulations, including DHARMA130b, which was omitted from previous plots for readability. In the baseline simulations (DHARMA260 and SAMEX260), drizzle depth below cloud base here appears roughly similar to that observed, but reflectivity is systematically biased low in DHARMA260. Halving the aerosol concentration (DHARMA130) results in a far deeper drizzle layer than observed, but reflectivity remains lesser than observed. If the number of bins is increased from 35 to 60 (corresponding to twice the spectral resolution), the resulting DHARMA130b simulation scarcely drizzles, indicating sensitivity to spectral resolution (not investigated in SAMEX), which is not uncommon in bin microphysics schemes (e.g., Prat et al. 2012) as discussed further below. If droplet concentration is additionally decreased to $65\,\mathrm{cm}^{-3}$ (DHARMA65b), reflectivity remains biased low, and drizzle still extends too far below cloud base. DHARMA results are qualitatively unaffected by adopting the Hall (1980) collection kernel, as in SAMEX. Thus, differences between DHARMA and SAMEX results appear to arise from differences in numerical implementation of the microphysical processes, potentially including elements of the droplet activation, growth and evaporation, sedimentation, and stochastic collection equation solution methods.

Figure 9 illustrates two higher radar moments: the mean Doppler velocity (vertical velocity weighted by reflectivity) and the Doppler spectral skewness (a measure of asymmetry in the spectrum). As illustrated further below, given a spectrum of motion from negative (downward) to positive (upward) velocity, a negative skewness indicates a prominent left-hand (negative) tail, whereas a positive skewness indicates a prominent right-hand (positive) tail. Given fixed air motion, a negative

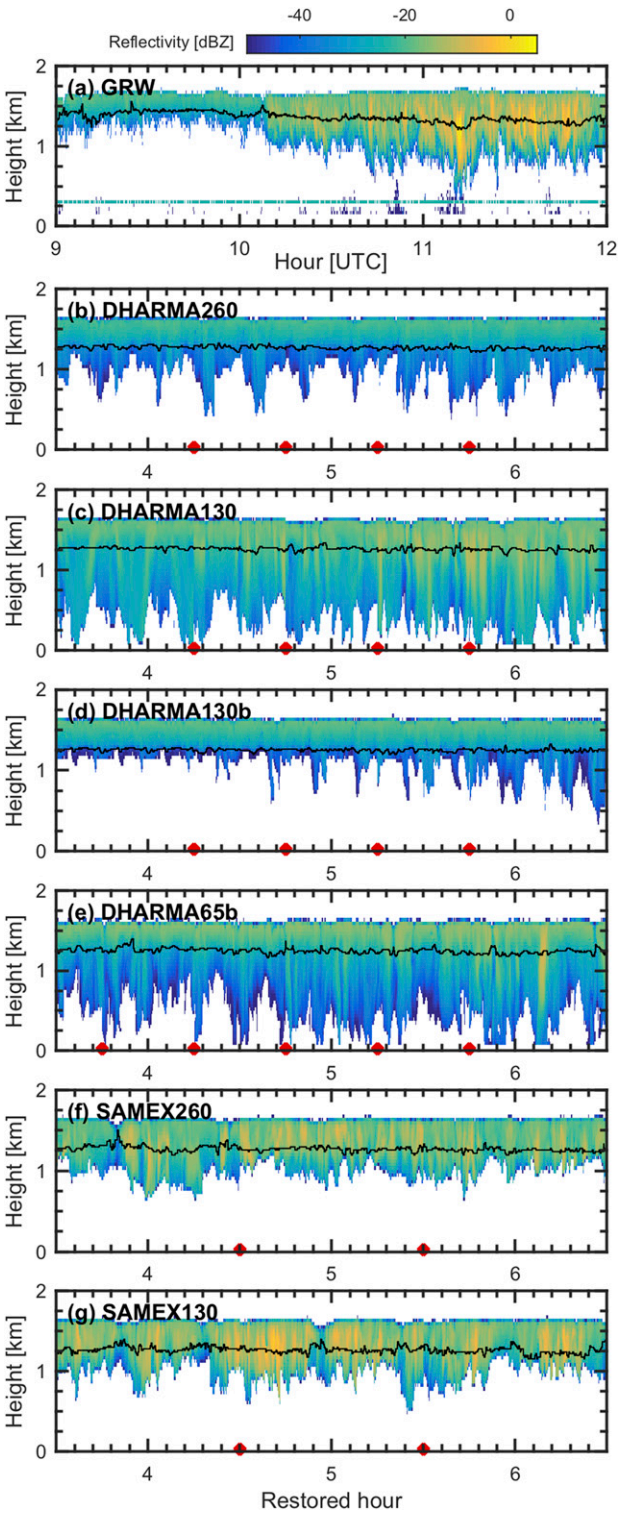

FIG. 8. Time–height plots of radar reflectivity (a) observed by the ground-based radar and (b)–(g) calculated from the last 2 h of six simulations. The simulated curtain plots are obtained by using the horizontal wind at CB to select the profiles that would be observed by a radar located mid-domain (see text). The red dots on the time axis indicate the change of domain (30-min domains for DHARMA and hourly domains for SAMEX). Black lines indicate CB observed by ceilometer or calculated from simulations (see text).

tail will be generated by the fastest falling drops (largest drizzle). The mean Doppler velocities forward calculated from all DHARMA simulations (see appendix A) tend to be too negative, and the skewness is far more negative than observed, especially below cloud base. Both SAMEX simulations better reproduce observed moment values, deviating primarily in skewness below cloud base, which does not stay positive enough. SAMEX also better reproduces the observed continuity of drizzle, whereas DHARMA drizzle shafts exhibit a more pronounced periodicity of roughly 15-min duration that is not seen in the observations, not that any such oscillations in a Lagrangian reference frame would be expected to be evident in an Eulerian one. In general, DHARMA biases are consistent with drizzle drops that are too large and require correspondingly longer distances to fully evaporate below cloud base. Increasing DHARMA's number of bins (decreasing the bin mass increments in DHARMA130b vs DHARMA130) decreases drizzle rate substantially but offers little improvement in moment values.

Figure 10 depicts the distribution of resolved vertical air motion above the cloud base as simulated and as retrieved from the WACR Doppler spectra for the whole day or the selected 6-h period following Kollias et al. (2001). Both models reproduce the vertical air motion distribution quite well, exhibiting downdrafts stronger than updrafts and more common upward motion, as observed. However, the distribution of simulated turbulence broadening (the turbulence contribution to Doppler spectral width) is wider than retrieved following Borque et al. (2016), especially in DHARMA, which predicts broadening values that are both smaller and larger than retrieved. In the retrievals, broadening is strongly peaked near $0.1\,\mathrm{m\,s^{-1}}$, with negligible values below $0.07\,\mathrm{m\,s^{-1}}$. In summary, here, we conclude that the resolved dynamics of the boundary layer is relatively well captured by both models. Below, we demonstrate that turbulence broadening differences are also not the primary source of differences between simulated and observed Doppler moment fields discussed thus far.

Figure 11 now moves further into the radar observational space by comparing relationships between the radar reflectivity, mean Doppler velocity, and spectral skewness. Median values are shown in 5-dB bins, and bins with less than 100 data points are excluded. In the observations, these relations are found to be notably

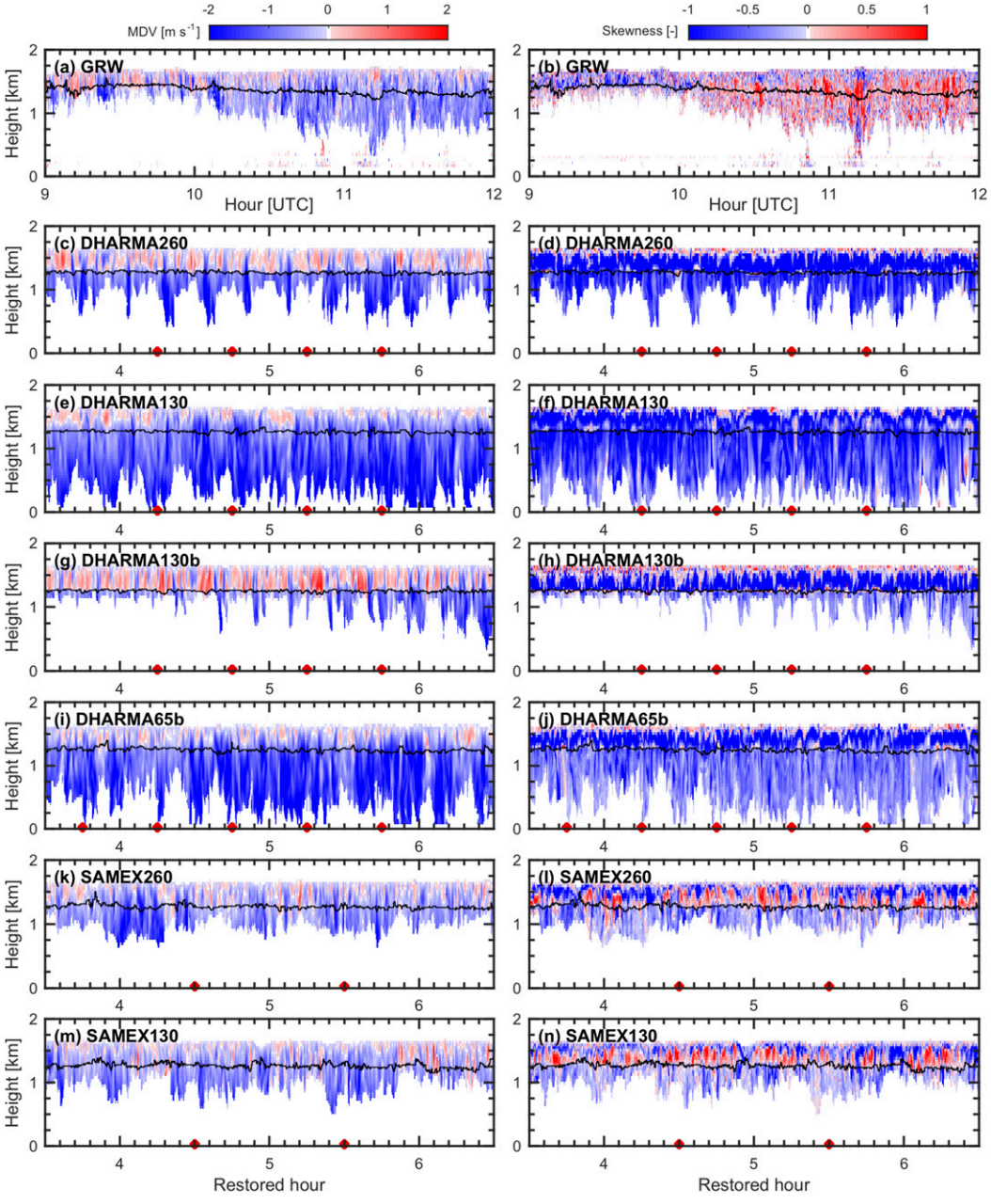

FIG. 9. As in Fig. 8, but for the radar (left) MDV and (right) spectral skewness. Sign convention is positive for upward motions.

similar across diverse locations and conditions (Kollias et al. 2011). For this study, they therefore serve as an initial benchmark for the models.

We consider first the evolution of mean Doppler velocity (MDV) in cloud as the reflectivity increases (Fig. 11a). In the observations, there is a monotonic increase of downward MDV with increasing reflectivity, starting at small downward motion and increasingly downward at an increasing rate. By contrast, both models produced pronounced minima of faster-than-observed downward MDV at reflectivities from −40 to −20 dBZ. This behavior occurs over a wider range of reflectivity in DHARMA, which also shows MDV then decreasing more rapidly than in SAMEX and observations. Just as the monotonic behavior in observations is commonly found in other datasets, the pronounced minimum in MDV at intermediate reflectivities is commonly found in DHARMA simulations of other

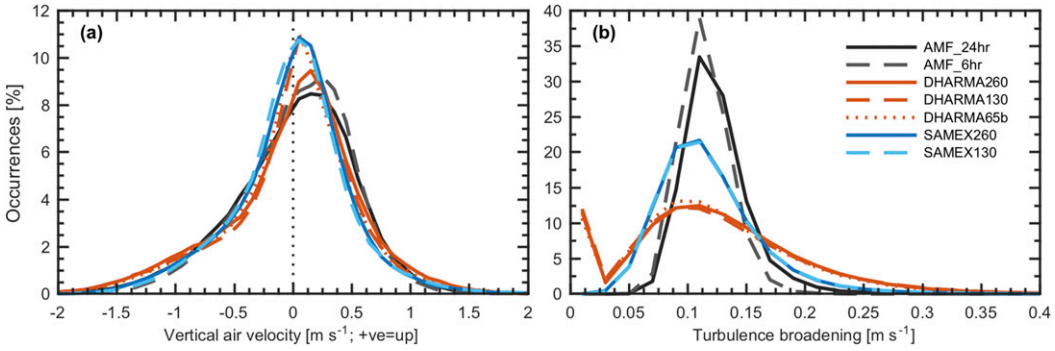

FIG. 10. Distributions of (a) vertical air velocity and (b) turbulence broadening above CB as retrieved by the cloud radar on Graciosa (whole day and 6 h are shown by the black solid and gray dashed lines, respectively) and obtained from five simulations (colored lines).

case studies (not shown). This pronounced and puzzling difference between fundamental moment relations in observations versus simulations at the outset of this study led to inclusion of SAMEX simulations, which surprisingly exhibit a similar discontinuity despite overall better agreement of the underlying moment values with observations shown thus far.

To investigate the differences seen in Fig. 11a, Figs. 11b and 11c decompose the MDV into reflectivity-weighted fall speed and vertical air motion, where simulated MDV is simply their sum and retrieved reflectivity-weighted fall speed is observed MDV minus retrieved vertical air motion (cf. Fig. 10). Here, we find another somewhat surprising result. Namely, whereas DHARMA overpredicts the median of reflectivity-weighted fall speeds at intermediate reflectivity values, SAMEX exhibits a greater commonality of downdrafts. Thus, it is curiously difficult for both models to reproduce this basic relationship of principal Doppler radar moments for differing reasons. Results are insensitive to minor differences between DHARMA and SAMEX drop fall speeds. In DHARMA, differences may be attributable primarily to the same factors responsible for biases in the underlying moment values.

We next consider the relationship of radar reflectivity with skewness in the Doppler spectra. Within the cloud layer, there are three regimes in the observations (Fig. 11d): (i) near-zero median skewness at the smallest reflectivities, (ii) slight negative skewness at intermediate reflectivities, and (iii) more strongly positive skewness at the largest reflectivities. These regimes are all reproduced in SAMEX simulations, although larger negative skewness values are attained, whereas DHARMA simulations

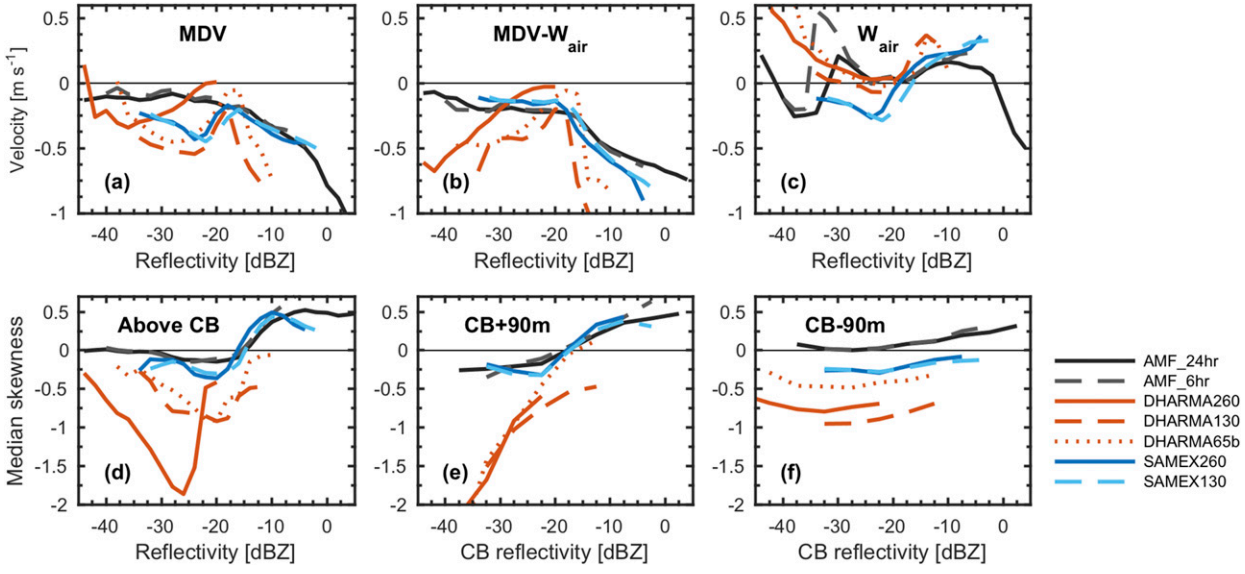

FIG. 11. Median values of in-cloud (a) MDV, (b) reflectivity-weighted fall speed, (c) vertical air motion, and (d) spectral skewness in simulations (blue and red; see legend) and radar measurements over the whole day and the selected 6-h period (black and gray). (e),(f) As in (d), but using CB reflectivity with the associated skewness values from 90 m above and below CB. All velocities are positive upward.

produce strongly negative median skewness values and never attain positive values.

Whereas in-cloud skewness reflects both cloud and drizzle size drops, skewness below cloud base reflects only drizzle properties. At two range gates above cloud base, Fig. 11e shows that all DHARMA simulations exhibit similar pronounced negative skewness with decreasing reflectivity. At two range gates below cloud base, Fig. 11f shows that all simulations exhibit a consistently negative bias in skewness relative to the radar observations at all reflectivities, consistent with a bias in the drizzle drop size distributions themselves, especially in DHARMA results, as discussed further below.

We have thus far found pronounced biases in forward-simulated radar observables, especially from DHARMA output. To more clearly guide future model development based on these relatively indirect observations, we next attempt to more firmly link the Doppler moment biases to underlying hydrometeor size distribution biases, focusing on the well observed region at cloud base (CB) and two range gates above cloud base (CB + 90 m). Figure 12 compares simulated number, mass, and reflectivity size distributions at both heights with in situ measurements selected from stratocumulus cloud-base measurements over the southeast Pacific (see appendix B), where CB and CB + 90 m are intended to roughly bound cloud-base sampling by aircraft. Simulated and observed size distributions are all normalized to facilitate comparison in Fig. 12. The two in situ size distributions were selected from all available Variability of American Monsoon Systems (VAMOS) Ocean–Cloud–Atmosphere–Land Study (VOCALS) cloud-base legs on the basis that they exhibit similar mass concentrations as all simulations above CB (Fig. 12b) and reflectivity on the upper end of that simulated (Fig. 12c); in addition, when reflectivity size distributions were plotted for all cloud-base legs, these appeared roughly continuous as in the simulations (which we take as an indication of robust sampling), with the exception of peaked excursions at diameters greater than 500 μm that were subjectively removed from the first leg shown. Despite roughly 50% greater total droplet number concentrations than any simulations, we also compare in situ number size distributions with those simulated. The number size distribution comparison is relevant to consider the drizzle size distribution shape (which dominates the reflectivity size distribution shape), but we do not expect vertical scaling to match (note y axis is log scale only in Figs. 12d and 12h). We note that extensive comparison of in situ size distributions is beyond the scope of this study, as discussed further below.

Considering number size distribution, an expected narrowing of the cloud droplet peak can be seen in simulations above cloud base (Fig. 12h vs Fig. 12d), and the observed peaks from each leg (plotted in both Figs. 12h and 12d for reference) appear more similar to those simulated at CB + 90 m. The in situ size distributions also peak at smaller sizes than simulated, consistent with higher total number concentrations. In the limit of large particles, the observed size distributions exhibit a sharp drop-off in the drizzle concentrations near a diameter of 200–300 μm, with a notable shoulder at 100–200 μm that is better reproduced by SAMEX than DHARMA. On a normalized basis, the number and mass contained in the shoulder size range is more pronounced in SAMEX than in the observations and DHARMA, but the SAMEX reflectivity distributions appear closely similar to observations as a function of both diameter and fall speed (Figs. 12j,k). When DHARMA produces sufficient drizzle particle numbers, similar to those in observations and SAMEX in the shoulder size range (in DHARMA130 and DHARMA65b), the drop-off in concentration at larger sizes is still not sharp enough, leading to excessive reflectivity contributed from drops with diameter larger than 300 μm. It appears that the shoulder feature may be common but variable in position and shape as a function of drop diameter and precipitation rate (e.g., Abel and Boutle 2012).

The forward-simulation process primarily subjects the reflectivity size distributions shown in Figs. 12g and 12k to dynamic broadening for comparison with observations. Figure 13 compares individual forward-simulated radar Doppler spectra with observations and selected simulations. A narrow range of reflectivity values around -25 dBZ is selected, and the vertical air motion is removed from each spectrum to facilitate comparison. We focus on range gates just above cloud base (CB + 90 m) and just below (CB − 90 m), where DHARMA's skewness is consistently biased negative (too many of the largest drizzle drops) and SAMEX's skewness transitions from relatively accurate values to a modest negative bias (cf. Figs. 11e,f). Individual observed spectra both above and below cloud base in Figs. 13a,b exhibit greater variability than individual simulated spectra (Figs. 13c–f). However, their composites appear narrower and more Gaussian in shape than those simulated, which are typical of other simulations from each model (Figs. 13g,h). In contrast to moment comparisons, the DHARMA65b and SAMEX130 spectra appear more similar to one another than to observations.

Above cloud base (Figs. 13c and 13e), both models exhibit pronounced condensation and drizzle modes, which are not seen in the observations (Fig. 13a) and which appear most prominent in simulated spectra with the most unrealistically large drizzle drops. The individual SAMEX spectra with the least large drizzle drops appear most similar to observations, with spectral power distributed smoothly from cloud droplet to drizzle drop sizes. Below cloud base, the observed

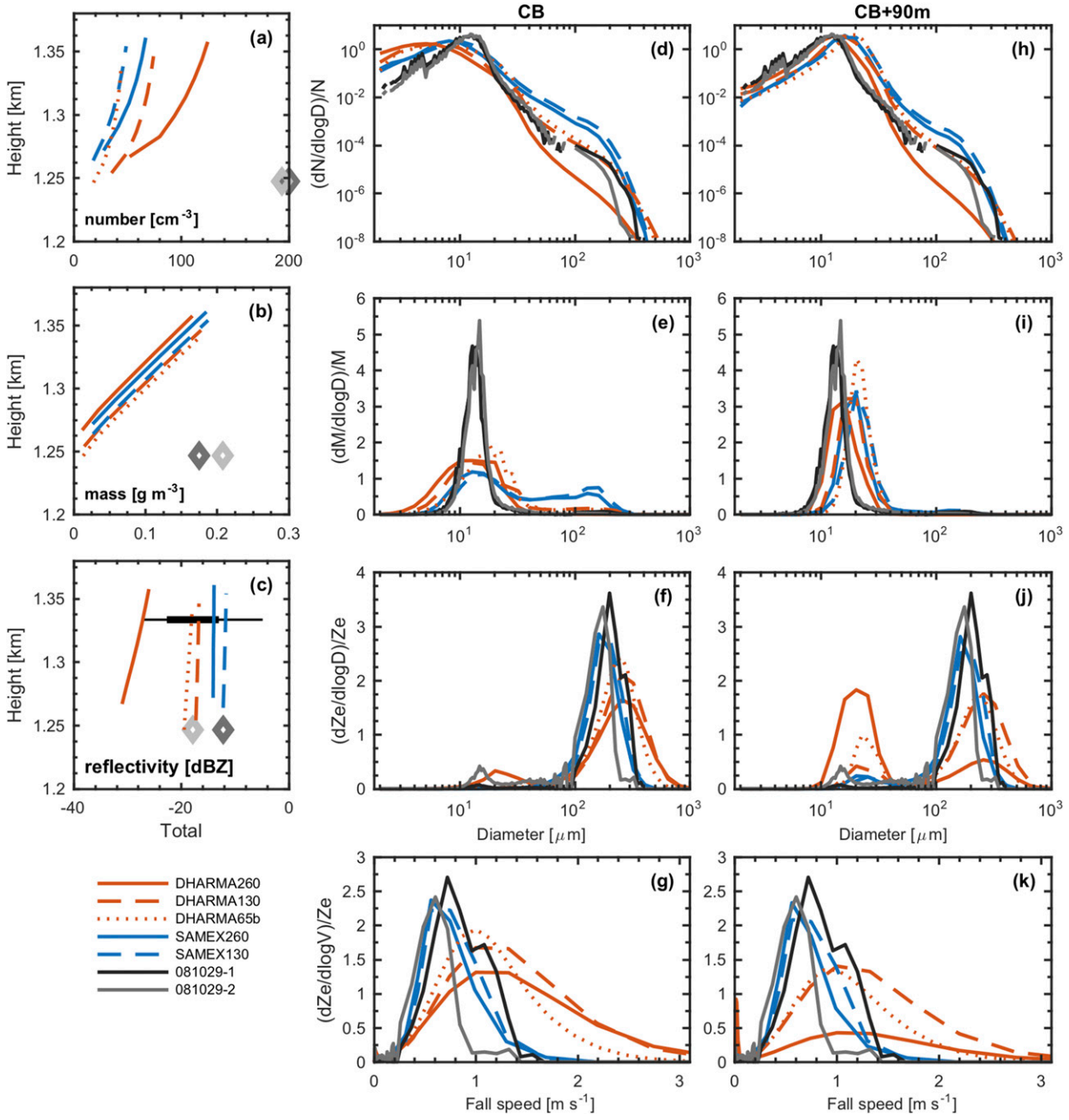

FIG. 12. (a) Total hydrometeor number concentration, (b) mass concentration, and (c) reflectivity corresponding to size distributions of number, mass, and reflectivity at (d)–(f) CB and (h)–(j) CB + 90 m in simulations (see legend). (g),(k) Reflectivity also shown as a function of hydrometeor fall speed. In situ observations are obtained from two flight legs near CB during VOCALS (see legend and text).

drizzle mode power spectrum peaks at $\sim 0.35\,\mathrm{m\,s^{-1}}$ (Fig. 13b). SAMEX matches that peak more closely than DHARMA (Fig. 13d vs Fig. 13f), but both models produce significant power at velocities roughly 2 times larger than those contributing significantly to observed power. This is especially true in DHARMA, where increasing the spectral resolution improves results only slightly (Figs. 13g,h), but also true in SAMEX. The more accurate skewness in SAMEX above cloud base than below (e.g., discontinuity at cloud base in Fig. 9h) is attributable to the largest fall speeds being offset by a tail on the positive end of the spectrum (Figs. 13g,h). In composite spectra at higher reflectivity ($-15\,\mathrm{dB}Z$ in Fig. 14), SAMEX more accurately produces the peak in spectral power at $\sim 0.5\,\mathrm{m\,s^{-1}}$ both above and below cloud base, but both models still produce substantial

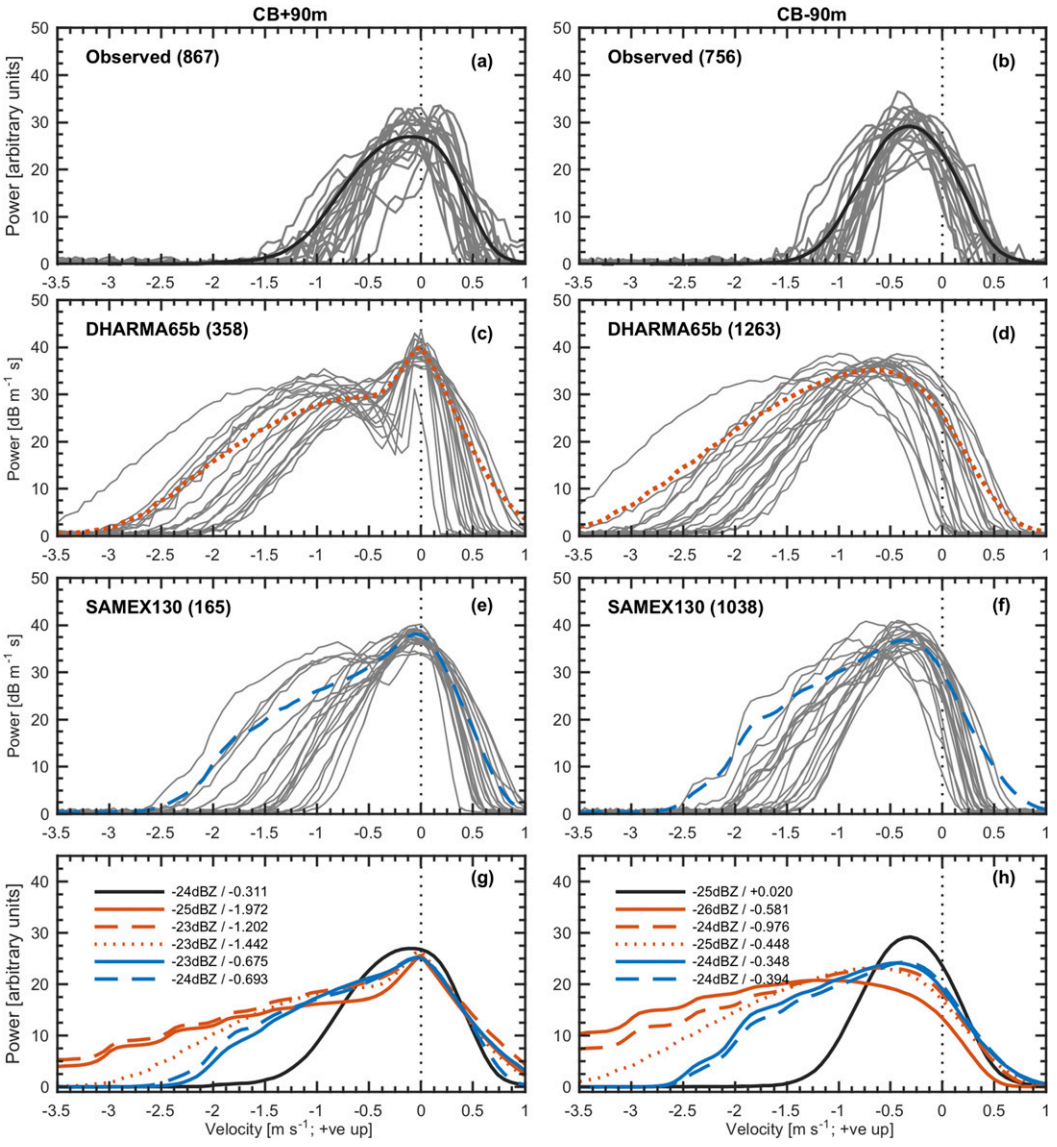

FIG. 13. Composite radar Doppler spectra at 90 m (left) above and (right) below CB where reflectivity is -25 ± 2.5 dBZ from (a),(b) 6-h observations, (c)–(f) DHARMA65b and SAMEX130 simulations, and (g),(h) other simulations (line types as in Fig. 12). Also shown in (a)–(f) are 20 individual contributing spectra (gray lines; randomly selected from the total number listed in parentheses). Composite reflectivity and skewness values are listed in (g) and (h).

power also at downward Doppler velocities much greater than observed.

5. Discussion and conclusions

A well-observed case study of persistent stratocumulus over the Azores is simulated using two independent LES models with bin microphysics. All simulations with both models (Table 1) produce nearly identical LWP and thermodynamic evolution over six hours (Fig. 4), but microphysics results differ substantially. In the baseline simulation ($N_a = 260\,\text{cm}^{-3}$), DHARMA droplet concentration (N_d) is 2 times that in SAMEX, and the drizzle rate at cloud base (P_{cb}) is only 10% of the value in SAMEX. DHARMA N_d is within 20% of that predicted by Abdul-Razzak and Ghan (2000) using the square root of the vertical wind speed variance at cloud base (CB) as an input, whereas SAMEX N_d is a factor of ~2.4 lower (Table 2). Given the differing predicted N_d and the nearly identical LWP values, SAMEX260 predicts P_{cb} roughly one-third that given by the Comstock et al. (2004) relation and DHARMA's is one-tenth of that from Comstock et al. (2004). With half as

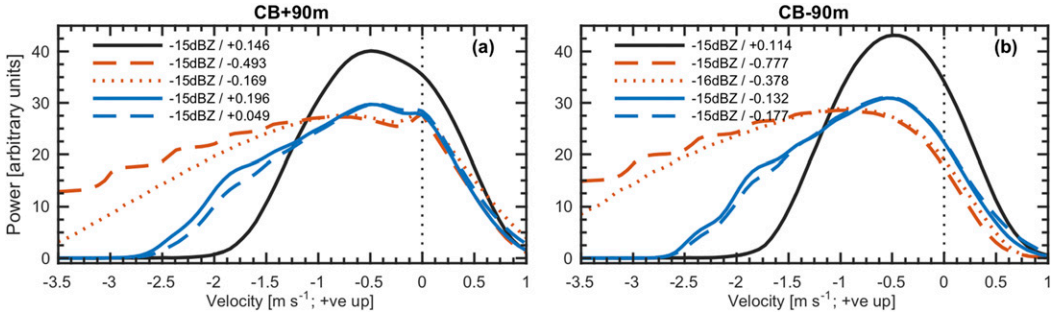

FIG. 14. As in Figs. 13g and 13h, but for points where reflectivity is -15 ± 2.5 dBZ. The DHARMA260 simulation is not shown because of an absence of values within that range.

many aerosol, DHARMA130 predicts N_d values similar to SAMEX260, with P_{cb} about one-eighth of that from Comstock et al. (2004). Within this context of substantially differing aerosol activation and drizzle formation in SAMEX and DHARMA, the remainder of this concluding section focuses on the size distributions of drizzle.

In comparison with cloud Doppler radar measurements, SAMEX drizzle is more realistic in many respects: drizzle is more continuous within the cloud layer, its rate is higher at CB and decreases more rapidly below CB, and Doppler spectra are less negatively skewed. A comparison of predicted size distributions with a few in situ data points provides some additional evidence that DHARMA does not reproduce a sharp drop-off in the number concentrations of drops larger than $\sim 200\,\mu$m (Fig. 12); the presence of droplets that are too large leads to the strong negative skewness in spectra that is also unrealistic in comparison with the radar observations. However, examination of individual forward-simulated spectra reveals that SAMEX exhibits similar behavior but to a lesser degree. Both models are unable to reproduce the basic monotonic trend of decreasing mean Doppler velocity (MDV) with increasing reflectivity that is consistently found in observations (Fig. 11a), SAMEX owing to biases in vertical air motion associated with intermediate reflectivity values and DHARMA owing to biases in MDV likely associated with excessive drizzle size. In DHARMA, excessive drizzle size is consistent with an unrealistically deep drizzle evaporation zone. These general conclusions are not sensitive to the precise radar observational period selected for comparison. Furthermore, it is apparent from variations in model setup beyond those documented here that DHARMA's biases in drizzle size distribution representation are indicative of the model's collision–coalescence scheme performance whenever drizzle is predicted and insensitive to other simulation details (e.g., aerosol properties, radiative transfer, activation scheme, and dynamics).

It is not surprising that models designed to simulate mass distributions may not be as well suited to predict reflectivity. In the case of DHARMA, the collision–coalescence solution method is designed for numerical stability and mass conservation in applications to multicomponent aerosol without special attention to limiting numerical diffusion (Jacobson et al. 1994; see also Jacobson 2011), whereas methods designed to limit numerical diffusion are less numerically stable, requiring short time steps, and may not conserve drop mass or number (e.g., Berry and Reinhardt 1974; Bott 2000). Here, we conclude that DHARMA requires a minimally diffusive collision–coalescence solution method in order to be used with cloud radar Doppler measurements to effectively study drizzle formation and evolution. Use of a hydrometeor size grid that is linear rather than geometric at the largest sizes (e.g., Prat et al. 2008) could also be required. It is further likely that if numerical diffusion is minimized, we may find that turbulence effects on the collision kernel or other modifications of the collision kernel itself or its solution scheme (e.g., Alfonso 2015; Lkhamjav et al. 2017) are necessary to reproduce properties of observations. We also cannot rule out a role for numerical diffusion associated with the droplet vapor growth scheme, which may be important to the supply of drizzle embryos. Preliminary results indicate that the DHARMA drizzle biases can be reproduced in box model simulations initialized with activated cloud droplets, where collision–coalescence is the only active process (not shown). It will be the objective of future work to use the observational targets supplied here as a guide for DHARMA scheme improvement under more realistic conditions.

A shortcoming of this study is a paucity of robust in situ measurements to directly support conclusions regarding errors in simulated drizzle size distributions. We examined a range of VOCALS and other in situ measurements with cloud-base flight legs but often

encountered gross discontinuities in calculated size-distributed reflectivity at large drop sizes. On one hand, we interpret such discontinuities as indicative of the challenge obtaining sufficient sample volume to measure statistically meaningful concentrations of the largest drops. On the other hand, individual spectra do reveal similar (but less pronounced) discontinuities at large drop sizes (cf. Fig. 13a), which suggest that drizzle distributions might be somewhat discontinuous within a radar sampling volume. A dedicated effort is required to critically evaluate the robustness and scale dependence of in situ measurements at cloud base used for comparisons with radar observations and models with far different sample volumes.

If model deficiencies are resolved (and we see no insurmountable barriers to that), this case study also suggests that cloud radar Doppler spectra and moment measurements in combination with LES with bin microphysics provides a powerful means for studying drizzle formation and evolution. Large domain simulations or simulations that incorporate mesoscale variability could address some shortfalls of the case-study approach here. From the observational standpoint, future datasets would benefit from in situ measurements of near-cloud aerosol and in-cloud droplet number concentrations in order to better evaluate each step in the simulated connections between aerosol, their activation, droplet size distributions, and drizzle properties.

Acknowledgments. This work was supported by the Office of Science (BER), U.S. Department of Energy, under Agreements DE-SC0006988 (PI Tselioudis), DE-SC0006736 (PI Mechem), DE-SC0013489 (ENA Site Science), and DE-SC0016237 (PI Fridlind) and by the NASA Radiation Sciences Program. Resources supporting this work were provided by the NASA High-End Computing (HEC) Program through the NASA Advanced Supercomputing (NAS) Division at Ames Research Center and by the National Energy Research Scientific Computing Center, a "user facility" supported by the Office of Science of the U.S. Department of Energy under Contract DE-AC02-05CH11231. CAP-MBL measurements were obtained from the Atmospheric Radiation Measurement (ARM) Program sponsored by the U.S. Department of Energy, Office of Science, Office of Biological and Environmental Research, Climate and Environmental Sciences Division. We acknowledge the use of Rapid Response imagery from the Land, Atmosphere Near real-time Capability for EOS (LANCE) system operated by the NASA GSFC Earth Science Data and Information System (ESDIS) with funding provided by NASA HQ. We thank Wanda Szyrmer for helpful discussion, Virendra Ghate for supporting radiative transfer calculations, Hyunho Lee for supporting box model simulations of collision–coalescence, and three anonymous referees for helpful comments.

APPENDIX A

Radar Simulator Description

The McGill Radar Doppler Spectra Simulator (MRDSS) is a simulator that emulates the measurements of a cloud Doppler radar using results from large-eddy simulations. MRDSS has two main modules: an instrument model and a forward model. Inputs to the instrument module are the radar characteristics, such as antenna pattern, pulse length, sensitivity, noise, and Doppler spectra parameters (Nyquist velocity, number of fast Fourier transform points, and spectral averages), and outputs are an accurate representation of the radar sampling volume and radar receiver. Inputs to the forward module are the simulated drop size distribution and the terminal fall speed as a function of drop size in each grid cell. Additional inputs are atmospheric state, including temperature, water vapor, horizontal and vertical wind speeds, and eddy dissipation rate. These parameters are used to simulate the propagation effects (i.e., attenuation), the electromagnetic scattering from the hydrometeors, and the Doppler shifts from the particle fall velocity, vertical air motion, and wind shear. Using these two modules, MRDSS outputs the Doppler spectrum and computed moments in each LES grid cell and at another desired vertical resolution.

The MRDSS forward model uses Mie theory to compute the backscatter cross section as a function of drop size. At this point, all drops are assumed to be spherical, since we are interested in drizzle processes and aspherical impacts are significant only for drops with a diameter of a few millimeters. Attenuation by gases (O_2 and H_2O) and liquid water are estimated at each grid cell, and their two-way effect is used to accurately simulate the radar signal attenuation. Gridcell dynamics are assumed to affect all drops equally, and the turbulence is assumed to be Gaussian. The vertical air motion simply shifts the whole spectrum, while wind shears, crosswinds, and turbulence are considered when broadening the peaks. Random noise consistent with radar-specific properties is added, and an ensemble of spectra is simulated for each grid cell and averaged together to smooth out some of the noise, following a radar's signal processing.

This method produces a Doppler spectrum within each simulation grid cell. If the radar range resolution is coarser than the model vertical resolution, a vertical stack of radar Doppler spectra are linearly averaged using the range weighting function to produce a final spectrum for comparison with the observations. When we use ARM profiling cloud radars, no horizontal averaging is assumed. This is supported by the short time

dwell of the ARM radars (1 s) and their very narrow beams that result in horizontal averaging lengths that are typically less than the horizontal model grid spacing. Given the difference between the vertically varying radar beamwidth (approximately 10 m near cloud base in this case) and the vertically uniform model horizontal grid mesh resolution (75 or 100 m in DHARMA and SAMEX simulations here), future simulator capabilities could include an operator designed to appropriately average the observations, as well. That was not attempted in this work but would not have changed the fundamental conclusions here regarding the most apparent model errors.

APPENDIX B

In Situ Measurements

In situ aircraft measurements are obtained from the VOCALS Regional Experiment (VOCALS-REx; Wood et al. 2011). From the Twin Otter aircraft (Zheng et al. 2011), we combine measurements from a phase Doppler interferometer (PDI; Chuang et al. 2008) and a cloud imaging probe (CIP; Baumgardner et al. 2001) as follows. The PDI samples drops of diameter $2 < D < 198\,\mu$m over 128 channels of constant logarithmic width $\Delta\log_{10}D = 0.0156$, and the CIP measures drops in the range $25 < D < 1550\,\mu$m over 62 channels of constant linear width 25 μm. Data from both probes are recorded at 1-Hz frequency. An instrument crossover diameter of 100 μm is chosen to optimize the effective sampling range of each instrument and avoid undesirable sizing uncertainty in CIP measurements for drops smaller than 100 μm (Strapp et al. 2001). The result is a combined size distribution using PDI channels 1–107 and CIP channels 4–62. While instantaneous measurements in the overlap range ($25 < D < 100\,\mu$m) sampled by both probes are not expected to match given the two instruments sampling different volumes, they show agreement when averaged over a typical flight leg.

This procedure resulted in a number of cloud-base flight legs. Of these, only two provided continuous or nearly continuous reflectivity size distributions without discontinuous and large excursions of high reflectivity that we take as an indication of insufficiently large sample volume for our purposes. Each size distribution is derived from an approximately 36-km leg targeting cloud base, spanning 1238:26–1248:56 and 1350:29–1400:42 UTC, respectively (081029-1 and 081029-2 in Fig. 12). The aircraft data presented here are freely available (https://www.eol.ucar.edu/field_projects/vocals).

REFERENCES

Abdul-Razzak, H., and S. J. Ghan, 2000: A parameterization of aerosol activation: 2. Multiple aerosol types. *J. Geophys. Res.*, **105**, 6837–6844, doi:10.1029/1999JD901161.

Abel, S. J., and I. A. Boutle, 2012: An improved representation of the raindrop size distribution for single-moment microphysics schemes. *Quart. J. Roy. Meteor. Soc.*, **138**, 2151–2162, doi:10.1002/qj.1949.

Ackerman, A. S., O. B. Toon, and P. V. Hobbs, 1993: Dissipation of marine stratiform clouds and collapse of the marine boundary layer due to the depletion of cloud condensation nuclei by clouds. *Science*, **262**, 226–229, doi:10.1126/science.262.5131.226.

——, ——, and ——, 1994: Reassessing the dependence of cloud condensation nucleus concentration on formation rate. *Nature*, **367**, 445–447, doi:10.1038/367445a0.

——, ——, and ——, 1995: A model for particle microphysics, turbulent mixing, and radiative transfer in the stratocumulus-topped marine boundary layer and comparisons with measurements. *J. Atmos. Sci.*, **52**, 1204–1236, doi:10.1175/1520-0469(1995)052<1204:AMFPMT>2.0.CO;2.

——, ——, D. E. Stevens, A. J. Heymsfield, V. Ramanathan, and E. J. Welton, 2000: Reduction of tropical cloudiness by soot. *Science*, **288**, 1042–1047, doi:10.1126/science.288.5468.1042.

——, M. P. Kirkpatrick, D. E. Stevens, and O. B. Toon, 2004: The impact of humidity above stratiform clouds on indirect aerosol climate forcing. *Nature*, **432**, 1014–1017, https://doi.org/10.1038/nature03174.

——, and Coauthors, 2009: Large-eddy simulations of a drizzling, stratocumulus-topped marine boundary layer. *Mon. Wea. Rev.*, **137**, 1083–1110, https://doi.org/10.1175/2008MWR2582.1.

Alfonso, L., 2015: An algorithm for the numerical solution of the multivariate master equation for stochastic coalescence. *Atmos. Chem. Phys.*, **15**, 12 315–12 326, doi:10.5194/acp-15-12315-2015.

Baumgardner, D., H. Jonsson, W. Dawson, D. O'Connor, and R. Newton, 2001: The cloud, aerosol and precipitation spectrometer: A new instrument for cloud investigations. *Atmos. Res.*, **59–60**, 251–264, doi:10.1016/S0169-8095(01)00119-3.

Beard, K. V., and H. T. Ochs, 1984: Collection and coalescence efficiencies for accretion. *J. Geophys. Res.*, **89**, 7165–7169, doi:10.1029/JD089iD05p07165.

Berry, E. X., and M. R. Pranger, 1974: Equations for calculating the terminal velocities of water drops. *J. Appl. Meteor.*, **13**, 108–113, doi:10.1175/1520-0450(1974)013<0108:EFCTTV>2.0.CO;2.

——, and R. L. Reinhardt, 1974: An analysis of cloud drop growth by collection. Part I: Double distributions. *J. Atmos. Sci.*, **31**, 1814–1824, doi:10.1175/1520-0469(1974)031<1814:AAOCDG>2.0.CO;2.

Böhm, J. P., 1999: Revision and clarification of "A general hydrodynamic theory for mixed-phase microphysics." *Atmos. Res.*, **52**, 167–176, doi:10.1016/S0169-8095(99)00033-2.

——, 2004: Reply to comment on "Revision and clarification of 'A general hydrodynamic theory for mixed-phase microphysics' [Böhm, J. P., 1999, Atmos. Res. 52, 167–176]." *Atmos. Res.*, **69**, 289–293, doi:10.1016/j.atmosres.2003.10.001.

Borque, P., E. Luke, and P. Kollias, 2016: On the unified estimation of turbulence eddy dissipation rate using Doppler cloud radars and lidars. *J. Geophys. Res. Atmos.*, **121**, 5972–5989, https://doi.org/10.1002/2015JD024543.

Bott, A., 2000: A flux method for the numerical solution of the stochastic collection equation: Extension to two-dimensional particle distributions. *J. Atmos. Sci.*, **57**, 284–294, doi:10.1175/1520-0469(2000)057<0284:AFMFTN>2.0.CO;2.

Chuang, P. Y., E. W. Saw, J. D. Small, R. A. Shaw, C. M. Sipperley, G. A. Payne, and W. D. Bachalo, 2008: Airborne phase Doppler interferometry for cloud microphysical measurements. *Aerosol Sci. Technol.*, **42**, 685–703, doi:10.1080/02786820802232956.

Clark, T. L., 1974: A study in cloud phase parameterization using the gamma distribution. *J. Atmos. Sci.*, **31**, 142–155, doi:10.1175/1520-0469(1974)031<0142:ASICPP>2.0.CO;2.

Colella, P., and P. R. Woodward, 1984: The piecewise parabolic method (PPM) for gas-dynamical simulations. *J. Comput. Phys.*, **54**, 174–201, doi:10.1016/0021-9991(84)90143-8.

Comstock, K. K., R. Wood, S. E. Yuter, and C. S. Bretherton, 2004: Reflectivity and rain rate in and below drizzling stratocumulus. *Quart. J. Roy. Meteor. Soc.*, **130**, 2891–2918, https://doi.org/10.1256/qj.03.187.

Deardorff, J. W., 1980: Stratocumulus-capped mixed layers derived from a three-dimensional model. *Bound.-Layer Meteor.*, **18**, 495–527, doi:10.1007/BF00119502.

Dee, D. P., and Coauthors, 2011: The ERA-Interim reanalysis: Configuration and performance of the data assimilation system. *Quart. J. Roy. Meteor. Soc.*, **137**, 553–597, doi:10.1002/qj.828.

Feingold, G., S. M. Kreidenweis, B. Stevens, and W. R. Cotton, 1996: Numerical simulations of stratocumulus processing of cloud condensation nuclei through collision–coalescence. *J. Geophys. Res.*, **101**, 21 391–21 402, doi:10.1029/96JD01552.

Green, A. W., 1975: An approximation for the shapes of large raindrops. *J. Appl. Meteor.*, **14**, 1578–1583, doi:10.1175/1520-0450(1975)014<1578:AAFTSO>2.0.CO;2.

Hall, W. D., 1980: A detailed microphysical model within a two-dimensional dynamical framework: Model description and preliminary results. *J. Atmos. Sci.*, **37**, 2486–2507, doi:10.1175/1520-0469(1980)037<2486:ADMMWA>2.0.CO;2.

Harrison, L., J. Michalsky, and J. Berndt, 1994: Automated multifilter rotating shadow-band radiometer: An instrument for optical depth and radiation measurements. *Appl. Opt.*, **33**, 5118–5125, doi:10.1364/AO.33.005118.

Hsieh, W. C., H. Jonsson, L.-P. Wang, G. Buzorius, R. C. Flagan, J. H. Seinfeld, and A. Nenes, 2009: On the representation of droplet coalescence and autoconversion: Evaluation using ambient cloud droplet size distributions. *J. Geophys. Res.*, **114**, D07201, https://doi.org/10.1029/2008JD010502.

Jacobson, M. Z., 2011: Numerical solution to drop coalescence/breakup with a volume-conserving, positive-definite, and unconditionally stable scheme. *J. Atmos. Sci.*, **68**, 334–346, doi:10.1175/2010JAS3605.1.

——, R. P. Turco, E. J. Jensen, and O. B. Toon, 1994: Modeling coagulation among particles of different composition and size. *Atmos. Environ.*, **28**, 1327–1338, doi:10.1016/1352-2310(94)90280-1.

Jensen, E. J., and Coauthors, 1998: Ice nucleation processes in upper tropospheric wave-clouds observed during SUCCESS. *Geophys. Res. Lett.*, **25**, 1363–1366, doi:10.1029/98GL00299.

Khairoutdinov, M., and Y. Kogan, 2000: A new cloud physics parameterization in a large-eddy simulation model of marine stratocumulus. *Mon. Wea. Rev.*, **128**, 229–243, doi:10.1175/1520-0493(2000)128<0229:ANCPPI>2.0.CO;2.

——, and D. A. Randall, 2003: Cloud resolving modeling of the ARM summer 1997 IOP: Model formulation, results, uncertainties, and sensitivities. *J. Atmos. Sci.*, **60**, 607–625, doi:10.1175/1520-0469(2003)060<0607:CRMOTA>2.0.CO;2.

Kirkpatrick, M. P., A. S. Ackerman, D. E. Stevens, and N. N. Mansour, 2006: On the application of the dynamic Smagorinsky model to large-eddy simulations of the cloud-topped atmospheric boundary layer. *J. Atmos. Sci.*, **63**, 526–546, doi:10.1175/JAS3651.1.

Kogan, Y. L., 1991: The simulation of a convective cloud in a 3-D model with explicit microphysics. Part I: Model description and sensitivity experiments. *J. Atmos. Sci.*, **48**, 1160–1189, doi:10.1175/1520-0469(1991)048<1160:TSOACC>2.0.CO;2.

——, D. B. Mechem, and K. Choi, 2012: Effects of sea-salt aerosols on precipitation in simulations of shallow cumulus. *J. Atmos. Sci.*, **69**, 463–483, doi:10.1175/JAS-D-11-031.1.

Kollias, P., B. A. Albrecht, R. Lhermitte, and A. Savtchenk, 2001: Radar observations of updrafts, downdrafts, and turbulence in fair-weather cumuli. *J. Atmos. Sci.*, **58**, 1750–1766, doi:10.1175/1520-0469(2001)058<1750:ROOUDA>2.0.CO;2.

——, W. Szyrmer, J. Rémillard, and E. Luke, 2011: Cloud radar Doppler spectra in drizzling stratiform clouds: 2. Observations and microphysical modeling of drizzle evolution. *J. Geophys. Res.*, **116**, D13203, doi:10.1029/2010JD015238.

Koren, I., and G. Feingold, 2011: Aerosol–cloud–precipitation system as a predator-prey problem. *Proc. Natl. Acad. Sci. USA*, **108**, 12 227–12 232, doi:10.1073/pnas.1101777108.

Larson, V. E., K. E. Kotenberg, and N. B. Wood, 2007: An analytic longwave radiation formula for liquid layer clouds. *Mon. Wea. Rev.*, **135**, 689–699, doi:10.1175/MWR3315.1.

Liu, Q.-F., Y. L. Kogan, D. K. Lilly, and M. P. Khairoutdinov, 1997: Variational optimization method for calculation of cloud drop growth in an Eulerian drop-size framework. *J. Atmos. Sci.*, **54**, 2493–2504, doi:10.1175/1520-0469(1997)054<2493:VOMFCO>2.0.CO;2.

Lkhamjav, J., H. Lee, Y.-L. Jeon, and J.-J. Baik, 2017: Examination of an improved quasi-stochastic model for the collisional growth of drops. *J. Geophys. Res. Atmos.*, **122**, 1713–1724, https://doi.org/10.1002/2016JD025904.

Long, C. N., and J. J. DeLuisi, 1998: Development of an automated hemispheric sky imager for cloud fraction retrievals. *Proc. 10th Symp. on Meteorological Observations and Instrumentation*, Phoenix, AZ, Amer. Meteor. Soc., 171–174.

Mead, J. B., and K. B. Widener, 2005: W-band ARM cloud radar. *32nd Int. Conf. on Radar Meteorology*, Albuquerque, NM, Amer. Meteor. Soc., P1R.3, http://ams.confex.com/ams/pdfpapers/95978.pdf.

Mechem, D. B., P. C. Robinson, and Y. L. Kogan, 2006: Processing of cloud condensation nuclei by collision-coalescence in a mesoscale model. *J. Geophys. Res.*, **111**, D18204, doi:10.1029/2006JD007183.

——, S. E. Yuter, and S. P. de Szoeke, 2012: Thermodynamic and aerosol controls in southeast Pacific stratocumulus. *J. Atmos. Sci.*, **69**, 1250–1266, doi:10.1175/JAS-D-11-0165.1.

——, S. E. Giangrande, C. S. Wittman, P. Borque, T. Toto, and P. Kollias, 2015: Insights from modeling and observational evaluation of a precipitating continental cumulus event observed during the MC3E field campaign. *J. Geophys. Res. Atmos.*, **120**, 1980–1995, https://doi.org/10.1002/2014JD022255.

Minnis, P., and Coauthors, 2011: CERES Edition-2 cloud property retrievals using TRMM VIRS and Terra and Aqua MODIS data—Part I: Algorithms. *IEEE Trans. Geosci. Remote Sens.*, **49**, 4374–4400, https://doi.org/10.1109/TGRS.2011.2144601.

Münkel, C., N. Eresmaa, J. Räsänen, and A. Karppinen, 2007: Retrieval of mixing height and dust concentration with lidar

ceilometer. *Bound.-Layer Meteor.*, **124**, 117–128, doi:10.1007/s10546-006-9103-3.

Prat, O. P., A. P. Barros, and C. R. Williams, 2008: An intercomparison of model simulations and VPR estimates of the vertical structure of warm stratiform rainfall during TWP-ICE. *J. Appl. Meteor. Climatol.*, **47**, 2797–2815, doi:10.1175/2008JAMC1801.1.

——, ——, and F. Y. Testik, 2012: On the influence of raindrop collision outcomes on equilibrium drop size distributions. *J. Atmos. Sci.*, **69**, 1534–1546, doi:10.1175/JAS-D-11-0192.1.

Rémillard, J., and G. Tselioudis, 2015: Cloud regime variability over the Azores and its application to climate model evaluation. *J. Climate*, **28**, 9707–9720, doi:10.1175/JCLI-D-15-0066.1.

Savic-Jovcic, V., and B. Stevens, 2008: The structure and mesoscale organization of precipitating stratocumulus. *J. Atmos. Sci.*, **65**, 1587–1605, doi:10.1175/2007JAS2456.1.

Smolarkiewicz, P. K., and W. W. Grabowski, 1990: The multidimensional positive definite advection transport algorithm: Nonoscillatory option. *J. Comput. Phys.*, **86**, 355–375, doi:10.1016/0021-9991(90)90105-A.

Stevens, B., W. R. Cotton, G. Feingold, and C.-H. Moeng, 1998: Large-eddy simulations of strongly precipitating, shallow, stratocumulus-topped boundary layers. *J. Atmos. Sci.*, **55**, 3616–3638, doi:10.1175/1520-0469(1998)055<3616:LESOSP>2.0.CO;2.

——, and Coauthors, 2003: Dynamics and chemistry of marine stratocumulus—DYCOMS-II. *Bull. Amer. Meteor. Soc.*, **84**, 579–593, doi:10.1175/BAMS-84-5-579.

Stevens, D. E., A. S. Ackerman, and C. S. Bretherton, 2002: Effects of domain size and numerical resolution on the simulation of shallow cumulus convection. *J. Atmos. Sci.*, **59**, 3285–3301, doi:10.1175/1520-0469(2002)059<3285:EODSAN>2.0.CO;2.

Strapp, J. W., F. Albers, A. Reuter, A. V. Korolev, U. Maixner, E. Rashke, and Z. Vukovic, 2001: Laboratory measurements of the response of a PMS OAP-2DC. *J. Atmos. Oceanic Technol.*, **18**, 1150–1170, doi:10.1175/1520-0426(2001)018<1150:LMOTRO>2.0.CO;2.

Suzuki, K., G. L. Stephens, S. C. van den Heever, and T. Y. Nakajima, 2011: Diagnosis of the warm rain process in cloud-resolving models using joint *CloudSat* and MODIS observations. *J. Atmos. Sci.*, **68**, 2655–2670, doi:10.1175/JAS-D-10-05026.1.

——, J.-C. Golaz, and G. L. Stephens, 2013: Evaluating cloud tuning in a climate model with satellite observations. *Geophys. Res. Lett.*, **40**, 4464–4468, doi:10.1002/grl.50874.

Tselioudis, G., W. Rossow, Y.-C. Zhang, and D. Konsta, 2013: Global weather states and their properties from passive and active satellite cloud retrievals. *J. Climate*, **26**, 7734–7746, doi:10.1175/JCLI-D-13-00024.1.

Turner, D. D., S. A. Clough, J. C. Liljegren, E. E. Clothiaux, K. E. Cady-Pereira, and K. L. Gaustad, 2007: Retrieving liquid water path and precipitable water vapor from the Atmospheric Radiation Measurement (ARM) microwave radiometers. *IEEE Trans. Geosci. Remote Sens.*, **45**, 3680–3690, doi:10.1109/TGRS.2007.903703.

VanZanten, M. C., B. Stevens, and G. Vali, 2005: Observations of drizzle in nocturnal marine stratocumulus. *J. Atmos. Sci.*, **62**, 88–106, doi:10.1175/JAS-3355.1.

——, and Coauthors, 2011: Controls on precipitation and cloudiness in simulations of trade-wind cumulus as observed during RICO. *J. Adv. Model. Earth Syst.*, **3**, M06001, https://doi.org/10.1029/2011MS000056.

Wang, H., and G. Feingold, 2009: Modeling mesoscale cellular structures and drizzle in marine stratocumulus. Part I: Impact of drizzle on the formation and evolution of open cells. *J. Atmos. Sci.*, **66**, 3237–3256, doi:10.1175/2009JAS3022.1.

Wood, R., 2005: Drizzle in stratiform boundary layer clouds. Part I: Vertical and horizontal structure. *J. Atmos. Sci.*, **62**, 3011–3033, doi:10.1175/JAS3529.1.

——, 2006: Rate of loss of cloud droplets by coalescence in warm clouds. *J. Geophys. Res.*, **111**, D21205, doi:10.1029/2006JD007553.

——, and Coauthors, 2011: The VAMOS Ocean-Cloud-Atmosphere-Land Study Regional Experiment (VOCALS-REx): Goals, platforms, and field operations. *Atmos. Chem. Phys.*, **11**, 627–654, https://doi.org/10.5194/acp-11-627-2011.

——, and Coauthors, 2015: Clouds, aerosols, and precipitation in the marine boundary layer: An ARM mobile facility deployment. *Bull. Amer. Meteor. Soc.*, **96**, 419–440, doi:10.1175/BAMS-D-13-00180.1.

——, J. D. Stemmler, J. Rémillard, and A. Jefferson, 2017: Low-CCN concentration air masses over the eastern North Atlantic: Seasonality, meteorology, and drivers. *J. Geophys. Res. Atmos.*, **122**, 1203–1223, https://doi.org/10.1002/2016JD025557.

Zheng, X., and Coauthors, 2011: Observations of the boundary layer, cloud, and aerosol variability in the southeast Pacific near-coastal marine stratocumulus during VOCALS-REx. *Atmos. Chem. Phys.*, **11**, 9943–9959, doi:10.5194/acp-11-9943-2011.